

Intraseasonal Sea-Level Variability in the Persian Gulf

Christopher G Piecuch^{1,1}, Ichiro Fukumori^{2,2}, and Rui M Ponte^{3,3}

¹Woods Hole Oceanographic Institution

²Jet Propulsion Laboratory

³Atmospheric and Environmental Research, Inc.

November 30, 2022

Abstract

Satellite observations are used to establish the dominant magnitudes, scales, and mechanisms of intraseasonal variability in ocean dynamic sea level (ζ) in the Persian Gulf over 2002-2015. Empirical orthogonal function (EOF) analysis applied to altimetry data reveals a basin-wide, single-signed intraseasonal fluctuation that contributes importantly to ζ variance in the Persian Gulf at monthly to decadal timescales. An EOF analysis of Gravity Recovery and Climate Experiment (GRACE) observations over the same period returns a similar large-scale mode of intraseasonal variability, suggesting that the basin-wide intraseasonal ζ variation has a predominantly barotropic nature. A linear barotropic theory is developed to interpret the data. The theory represents Persian-Gulf-average ζ (ζ) in terms of local freshwater flux, barometric pressure, and wind stress forcing, as well as ζ at the boundary in the Gulf of Oman. The theory is tested using a multiple linear regression with these freshwater flux, barometric pressure, wind stress, and boundary ζ quantities as input, and as output. The regression explains 70% +/- 9% (95% confidence interval) of the intraseasonal variance. Numerical values of regression coefficients computed empirically from the data are consistent with theoretical expectations from the theory. Results point to a substantial non-isostatic response to surface loading. The Gulf of Oman ζ boundary condition shows lagged correlation with ζ upstream along the Indian Subcontinent, Maritime Continent, and equatorial Indian Ocean, suggesting a large-scale Indian-Ocean influence on intraseasonal variation mediated by coastal and equatorial waves, and hinting at potential predictability. This study highlights the value of GRACE for understanding sea level in an understudied marginal sea.

1 **Coversheet for “Intraseasonal Sea-Level Variability in the**
2 **Persian Gulf”**

3 Christopher G. Piecuch^{1,†}, Ichiro Fukumori^{2,‡}, & Rui M. Ponte^{3,*}

4 ¹*Woods Hole Oceanographic Institution, Woods Hole, Massachusetts, USA*

5 ²*Jet Propulsion Laboratory, Pasadena, California, USA*

6 ³*Atmospheric and Environmental Research, Inc., Lexington, Massachusetts, USA*

7 This is a preprint submitted to Earth and Space Science Open Archive (ESSOAr). This paper
8 been peer reviewed and accepted at Journal of Physical Oceanography. Copyright in this work may
9 be transferred without further notice.

10 † cpiecuch@whoi.edu

11 ‡ ichiro.fukumori@jpl.nasa.gov

12 * rponte@aer.com

1 **Intraseasonal Sea-Level Variability in the Persian Gulf**

2 Christopher G. Piecuch*

3 *Woods Hole Oceanographic Institution, Woods Hole, Massachusetts, USA*

4 Ichiro Fukumori

5 *Jet Propulsion Laboratory, Pasadena, California, USA*

6 Rui M. Ponte

7 *Atmospheric and Environmental Research, Inc., Lexington, Massachusetts, USA*

8 *Corresponding author: Christopher G. Piecuch, cpiecuch@whoi.edu

ABSTRACT

9 Satellite observations are used to establish the dominant magnitudes, scales, and mechanisms
10 of intraseasonal variability in ocean dynamic sea level (ζ) in the Persian Gulf over 2002–2015.
11 Empirical orthogonal function (EOF) analysis applied to altimetry data reveals a basin-wide, single-
12 signed intraseasonal fluctuation that contributes importantly to ζ variance in the Persian Gulf at
13 monthly to decadal timescales. An EOF analysis of Gravity Recovery and Climate Experiment
14 (GRACE) observations over the same period returns a similar large-scale mode of intraseasonal
15 variability, suggesting that the basin-wide intraseasonal ζ variation has a predominantly barotropic
16 nature. A linear barotropic theory is developed to interpret the data. The theory represents
17 Persian-Gulf-average ζ ($\bar{\zeta}$) in terms of local freshwater flux, barometric pressure, and wind stress
18 forcing, as well as ζ at the boundary in the Gulf of Oman. The theory is tested using a multiple
19 linear regression with these freshwater flux, barometric pressure, wind stress, and boundary ζ
20 quantities as input, and $\bar{\zeta}$ as output. The regression explains $70\% \pm 9\%$ (95% confidence interval)
21 of the intraseasonal $\bar{\zeta}$ variance. Numerical values of regression coefficients computed empirically
22 from the data are consistent with theoretical expectations from first principles. Results point to
23 a substantial non-isostatic response to surface loading. The Gulf of Oman ζ boundary condition
24 shows lagged correlation with ζ upstream along the Indian Subcontinent, Maritime Continent,
25 and equatorial Indian Ocean, suggesting a large-scale Indian-Ocean influence on intraseasonal $\bar{\zeta}$
26 variation mediated by coastal and equatorial waves, and hinting at potential predictability. This
27 study highlights the value of GRACE for understanding sea level in an understudied marginal sea.

28 **1. Introduction**

29 The Persian Gulf¹ is a semi-enclosed marginal sea of the Indian Ocean (Figure 1). It connects to
30 the Arabian Sea to the southeast through the Strait of Hormuz and the Gulf of Oman. The Persian
31 Gulf is shallow and broad, with an average depth of ~ 30 m and a surface area of $\sim 2.2 \times 10^5$ km².
32 It is subject to an arid, subtropical climate, and is bounded to the southwest by the Arabian Desert
33 and by the Zagros mountains to the northeast.

34 Past studies establish the basic physical oceanography of the Persian Gulf using data and models
35 (Chao et al., 1992; Emery, 1956; Johns et al., 1999, 2003; Kämpf and Sadrinasab, 2006; Reynolds,
36 1993; Thoppil and Hogan, 2010; Swift and Bower, 2003; Yao and Johns, 2010). We outline some
37 of the salient features for context. The region is forced year-round by north-northwesterly surface
38 winds ('shamal', speeds 3–6 m s⁻¹). Evaporation (~ 2 m y⁻¹) far exceeds precipitation and runoff
39 (~ 0.2 m y⁻¹), resulting in an inverse-estuarine circulation—fresher, warmer buoyant waters inflow
40 near the surface through the Strait of Hormuz largely along the coast of Iran, whereas saltier, colder,
41 denser waters outflow near the bottom mainly along the coast of the United Arab Emirates. The
42 basin-scale circulation is demarcated by a thermal front across the Persian Gulf between Qatar and
43 Iran. Northwest of the front, there is equatorward flow along Saudi Arabia driven by wind-forced
44 downwelling at the coast and buoyant river discharge from the Tigris, Euphrates, and other rivers
45 at the head of the Persian Gulf. To the southeast, there exists a large-scale counterclockwise
46 circulation, maintained by exchanges through the Strait of Hormuz, and evaporation, cooling, and
47 sinking of water masses in shallow regions along the southern Persian Gulf. Mesoscale eddies are
48 common, especially during boreal summer, when they are shed from the Iranian Coastal Jet due to
49 baroclinic instability. There is a seasonal cycle in the vertical stratification, such that top-to-bottom

¹The name of this body of water is subject to dispute. It is also known as the Arabian Gulf or the Gulf. We use the name Persian Gulf following the conventions of the International Hydrographic Organization and the United Nations.

50 potential density contrasts are weaker in winter ($0\text{--}1\text{ kg m}^{-3}$) and stronger in summer ($2\text{--}5\text{ kg m}^{-3}$).
51 For more details, interested readers are directed to the papers cited above.

52 The Persian Gulf is one of the world ocean's busiest waterways, due to its vast oil and gas stores,
53 which are of longstanding geopolitical, economic, and military interest (al-Chalabi, 2007; Barnes
54 and Myers Jaffe, 2006; Larson, 2007). Bordering eight nations, the Persian Gulf is also home to
55 large coastal populations and major coastal cities including Dubai, Abu Dhabi, and Doha, which
56 are exposed to risk of flooding and inundation related to sea-level change (Al-Jeneid et al., 2008;
57 Lafta et al., 2020). Kopp et al. (2014, 2017) project that mean sea level will rise by 44–108 cm
58 between 2000 and 2100 in Bahrain under the Representative Concentration Pathway 8.5 forcing
59 scenario (66% confidence). This would threaten $\sim 10\text{--}15\%$ ($\sim 80\text{--}100\text{ km}^2$) of Bahrain's surface
60 area (Al-Jeneid et al., 2008). Such numbers emphasize the importance of understanding sea-level
61 changes in the Persian Gulf. However, projections of mean sea-level rise on multidecadal and longer
62 timescales (Kopp et al., 2014, 2017) alone are insufficient to anticipate future coastal flood risk.
63 Also important are sea-level fluctuations at decadal and shorter periods, which can superimpose
64 on longer-term changes, temporarily ameliorating or exacerbating coastal risk (Burgos et al., 2018;
65 Dangendorf et al., 2016; Long et al., 2020; Ray and Foster, 2016; Sweet et al., 2017). This
66 motivates a detailed investigation of mean sea-level variation in the Persian Gulf on decadal and
67 shorter timescales—what are the dominant magnitudes, scales, and mechanisms?

68 Past studies on Persian Gulf mean sea level largely focus on seasonal cycles and decadal trends
69 (Al-Subhi, 2010; Alothman et al., 2014; Ayhan, 2020; Barzandeh et al., 2018; El-Gindy, 1991;
70 El-Gindy and Eid, 1997; Hassanzadeh et al., 2007; Hosseinibalam et al., 2007; Sharaf El Din,
71 1990; Siddig et al., 2019; Sultan et al., 1995a, 2000). Sultan et al. (1995a) consider monthly
72 relative sea level during 1980–1990 from two tide gauges on the Saudi Arabia coast. They find
73 that 80% of the overall monthly data variance is explained by the seasonal cycle, which has an

74 amplitude of ~ 10 cm and peaks in boreal summer. These authors argue that 75% of the seasonal
75 variance in sea level reflects an inverted-barometer response to a ~ 10 -mb-amplitude seasonal cycle
76 in local surface air pressure, and that the remaining 25% of seasonal variance represents steric
77 variability owing to density fluctuations. Other studies targeting different regions, tide gauges, and
78 time periods confirm this basic result that inverted-barometer and steric effects make primary and
79 secondary contributions, respectively, to the large-scale seasonal cycle in Persian Gulf sea level,
80 but also suggest that local wind effects are important in some places (Al-Subhi, 2010; Barzandeh
81 et al., 2018; El-Gindy, 1991; El-Gindy and Eid, 1997; Hassanzadeh et al., 2007; Hosseinibalam et
82 al., 2007; Sharaf El Din, 1990; Sultan et al., 2000). Alothman et al. (2014) interrogate monthly
83 relative sea level over 1979–2007 based on 15 tide-gauge records from Bahrain, Saudi Arabia, and
84 Iran, along with measurements of vertical land motion from 6 Global Positioning System (GPS)
85 stations in Bahrain, Saudi Arabia, and Kuwait. They determine that regional relative sea level rose
86 by 2.2 ± 0.5 mm y^{-1} over that time. These authors find that one-third of the increase (0.7 ± 0.6 mm
87 y^{-1}) was due to crustal subsidence, possibly related to groundwater pumping and oil extraction
88 (Amin and Bankher, 1997), and the remaining two-thirds (1.5 ± 0.8 mm y^{-1}) was due to geocentric
89 sea-level changes. Sultan et al. (2000) calculate a more muted relative sea-level trend (1.7 mm
90 y^{-1}) based on 9 tide-gauge records from Saudi Arabia over 1980–1994, while Siddig et al. (2019)
91 estimate a larger geocentric sea-level trend (3.6 ± 0.4 mm y^{-1}) from altimetry data averaged over
92 the Persian Gulf during 1993–2018, consistent with reports of a global sea-level acceleration in
93 recent decades (Nerem et al., 2018; Dangendorf et al., 2019; Frederikse et al., 2020).

94 Omitted from past works on Persian Gulf mean sea level is exploration of nonseasonal sea-level
95 variation. This is an important omission, since nonseasonal variations in general, and in particular
96 intraseasonal variations, contribute importantly to mean sea-level variance over the Persian Gulf on
97 monthly to decadal timescales. For example, consider the time series of monthly ocean dynamic

98 sea level² from satellite-altimetry data averaged over the Persian Gulf during 2002–2015 shown in
99 Figure 2. Filters are applied to the data to emphasize variability on different timescales, and global-
100 mean sea level and the inverted-barometer effect are removed. Nonseasonal fluctuations explain
101 52% of the monthly data variance, and intraseasonal fluctuations (with ~ 2–6-month periods) alone
102 account for 46% of the overall data variance. The altimetric time series of intraseasonal sea level
103 averaged over the Persian Gulf also explains 51% of the intraseasonal variance in relative sea level
104 averaged across 5 tide gauges from Iran and Bahrain during the overlapping period 2002–2006
105 (Figure 2). This exploratory analysis suggests that large-scale intraseasonal fluctuations make
106 important contributions to ocean dynamic sea-level variance across the Persian Gulf during the
107 altimeter era, motivating a more in-depth investigation.

108 Here we investigate the magnitudes, scales, and mechanisms of intraseasonal sea-level variability
109 in the Persian Gulf through an analysis of satellite observations, tide gauges, reanalysis products,
110 and gridded surface flux estimates. The remainder of the paper is structured as follows: in section
111 2, we describe the data; in section 3, we establish the horizontal scales and vertical structure of
112 the dominant intraseasonal sea-level variation in the Persian Gulf; in section 4, we use dynamical
113 theory, linear regression, and correlation analysis to identify the main local and nonlocal forcing
114 mechanisms and ocean dynamics responsible for driving intraseasonal variations in Persian Gulf
115 sea level and their relation to large-scale circulation and climate in the Equatorial and North Indian
116 Ocean; we conclude with a summary and discussion in section 5.

²Ocean dynamic sea level is the local height of the sea surface above the geoid adjusted for the inverted-barometer effect (Gregory et al., 2019).

117 2. Materials and Methods

118 a. Ocean dynamic sea level from satellite altimetry

119 We use version 2.0 of the sea-level essential climate variable product from the European Space
120 Agency Climate Change Initiative (Legeais et al., 2018; Quartly et al., 2017). Data were down-
121 loaded from the Centre for Environmental Data Analysis on 18 April 2020. (All data sources are
122 indicated in Table 1.) The multi-satellite merged geocentric sea-level anomalies are given on a
123 0.25° global spatial grid and a monthly time increment during 1993–2015. These data extend and
124 update the earlier version 1.1 product (Ablain et al., 2015). The dynamic atmospheric correction
125 is applied, which involves removing the ocean’s dynamic barotropic response to wind and pressure
126 forcing at shorter periods < 20 days and its isostatic response to pressure forcing at longer periods
127 > 20 days from the data (Carrère and Lyard, 2003; Carrère et al. 2016). (The dynamic ocean
128 response to these forcings at the periods of interest to this study are retained in the data.) For
129 more details on the geophysical corrections, orbit solutions, altimeter standards, and error budgets,
130 see Quartly et al. (2017) and Legeais et al. (2018). We remove the time series of global-mean
131 geocentric sea-level values from every grid cell, and the resulting sea-level anomalies mainly reflect
132 ocean dynamic sea-level anomalies. [We do not adjust the altimetry, or any other dataset, for the
133 spatially variable effects of gravitation, rotation, and deformation related to contemporary surface
134 ice and water mass redistribution, since these effects are negligible in this area on these timescales
135 (Adhikari et al., 2019).] We use these data from May 2002 to September 2015, which corresponds
136 roughly to the quasi-continuous Gravity Recovery and Climate Experiment (GRACE) record that
137 is used for interpretation and described below. Following Gregory et al. (2019), we use ζ to denote
138 ocean dynamic sea level.

139 This paper focuses on intraseasonal variability. To isolate intraseasonal behavior, we process
140 the data as follows. We use least squares to estimate the seasonal cycle (annual and semi-annual
141 sinusoids) and linear trend in the data over the study period. We then remove these seasonal and
142 trend contributions from the original data to create a time series of nonseasonal residuals. Next, we
143 apply a Gaussian smoother with a 3-month half window to these nonseasonal residuals. Finally,
144 we subtract this low-pass-filtered time series from the nonseasonal residuals to create a record of
145 intraseasonal fluctuations, which is the object of our study. We delete the first and last 6 months of
146 the intraseasonal time series to avoid edge effects. This filter passes $> 90\%$ of the power at periods
147 $\lesssim 8$ months and stops $> 70\%$ of the power at periods $\gtrsim 15$ months. See Figure 2 for an example of
148 this filtering applied to altimetry averaged over the Persian Gulf.

149 *b. Manometric sea level from satellite gravimetry*

150 We consider data from GRACE and GRACE Follow-On (Landerer et al., 2020; Watkins et al.,
151 2015; Wiese et al., 2016). Mass grids were downloaded from the National Aeronautics and Space
152 Administration Jet Propulsion Laboratory on 15 April 2020 (data version JPL RL06M.MSCNv02).
153 The data are processed using 3° spherical-cap mass-concentration blocks for the gravity-field basis
154 functions. For more details on the estimation process, spatial constraints, scale factors, and leakage
155 errors, see Watkins et al. (2015). The data are defined on a 0.5° global spatial grid, but the satellite
156 measurement do not resolve processes with spatial scales $\lesssim 300$ km. We use the version of the
157 data with the coastline resolution improvement filter applied (Wiese et al., 2016). The grids are
158 defined at irregular, quasi-monthly increments, and have gaps. For example, battery management
159 issues caused multi-month data gaps in the final years of GRACE, and there is a ~ 1 -y data gap
160 between the end of GRACE coverage and the beginning of the GRACE Follow-On record. We
161 linearly interpolate the available ocean mass grids onto regular monthly increments from May 2002

162 through September 2015. The data have units of equivalent water thickness. After correcting for
163 global air-pressure effects, these data reflect manometric sea-level anomalies³. To isolate dynamic
164 manometric sea-level anomalies associated with internal ocean mass redistribution, we subtract the
165 time series of barystatic sea level⁴ from the data at every oceanic grid cell. Intraseasonal variations
166 are isolated through filtering methods described earlier. Following Gregory et al. (2019), we use
167 R_m to indicate manometric sea level, with its dynamic nature understood.

168 *c. Relative sea level from tide gauges*

169 We also use monthly mean relative sea level⁵ from tide-gauge records in the Persian Gulf that
170 overlap with our study period (Table 2). Data were downloaded from the Permanent Service
171 for Mean Sea Level database on 1 July 2019 (PSMSL, 2019; Holgate et al., 2013). The data
172 from Mina Sulman in Manama, Bahrain represent the only record from the Persian Gulf in the
173 PSMSL database with a complete benchmark datum history (so-called revised local reference
174 data). To consider large-scale regional behavior, we also study a careful selection of records
175 without continuous datum histories (so-called metric data). Namely, we use the data from Emam
176 Hassan, Bushehr, Kangan, and Shahid Rajaee in Iran⁶. We consider the data over 2002–2006, since
177 earlier times predate our study, and later times feature no tide-gauge data (Table 2). The data from
178 Emam Hassan before November 2002 are omitted due to a data gap that coincided with an apparent
179 datum shift (Allothman et al., 2014). We adjust each record for the inverted-barometer effect using

³Manometric sea-level changes indicate sea-level changes due to changes in the local mass of the ocean per unit area (Gregory et al., 2019).

⁴Barystatic sea-level changes refer to global-mean manometric sea-level changes and correspond to net addition or subtraction of water mass to or from the global ocean (Gregory et al., 2019).

⁵Relative sea level is the height of the sea surface relative to the solid Earth (Gregory et al., 2019).

⁶Metric data from other Persian Gulf locations are also available in the PSMSL database. However, we determined that these records were unsuitable for our analysis. Five records from the United Arab Emirates, Qatar, and Iraq are short and predate our study period. A dozen records from Saudi Arabia were operated by the Saudi Arabian Oil Company and situated on oil platforms, and are therefore potentially unstable.

180 reanalysis surface air pressure (see below). Next, we remove the seasonal cycle and linear trend
181 from each adjusted time series. We then average together these nonseasonal time series to create
182 a regional composite of adjusted relative sea level. Finally, we isolate intraseasonal variability by
183 computing and then removing a low-pass-filtered version of the regional composite. The resulting
184 time series is shown in Figure 2. To the extent that global-mean sea-level changes are unimportant,
185 this composite time series represents tide-gauge-based intraseasonal regional ζ variability.

186 To establish regional context, we also consider all 53 monthly mean relative sea-level records in
187 the PSMSL revised local reference database in the Equatorial and North Indian Ocean (40–105°E,
188 12.5°S–32.5°N) with ≥ 84 months of data during 2002–2015 ($\geq 50\%$ data completeness over the
189 study period). These data are also adjusted for the inverted-barometer effect and filtered to isolate
190 intraseasonal behavior as described above.

191 *d. Surface forcing*

192 We use gridded observations, atmospheric reanalyses, and flux estimates to interpret the data
193 from altimetry, GRACE, and tide gauges. For all fields, we compute intraseasonal anomalies
194 during 2002–2015 from the available monthly values, as with the altimetry and GRACE.

195 We use monthly wind stress and barometric pressure from the European Centre for Medium Range
196 Weather Forecasts Reanalysis Interim (ERA-Interim; Dee et al., 2011). Fields were downloaded
197 from the Woods Hole Oceanographic Institution (WHOI) Community Storage Server on 7 January
198 2019. Values are defined on a 0.75° global spatial grid from January 1979 to October 2018.

199 We use monthly evaporation from version 3 of the the Objectively Analyzed air-sea Fluxes project
200 (OAFlux; Yu and Weller, 2007). Fields were downloaded from WHOI servers on 13 November
201 2019. Values are defined on a 1° global spatial grid from January 1958 to December 2018.

202 We use monthly precipitation from version 2.3 of the Global Precipitation Climatology Project
203 (GPCP; Adler et al., 2003). Fields were downloaded from National Oceanic and Atmospheric
204 Administration Earth System Research Laboratory and Physical Sciences Laboratory on 16 April
205 2020. Values are defined on a 2.5° global spatial grid from January 1979 to the present.

206 We use monthly river runoff from the Japanese 55-year atmospheric reanalysis surface data set
207 for driving ocean–sea-ice models (JRA55-do; Tsujino et al., 2018). Fields were downloaded from
208 servers at the Hokkaido University Graduate School of Environmental Science on 21 August 2020.
209 Values are defined on a 0.25° global coastal grid from January 1958 to December 2017.

210 **3. Horizontal scales and vertical structure of ζ variability**

211 Past studies use satellite altimetry and tide gauges to study seasonal cycles and decadal trends in
212 the Persian Gulf (Al-Subhi, 2010; Alothman et al., 2014; Ayhan, 2020; El-Gindy, 1991; El-Gindy
213 and Eid, 1997; Hassanzadeh et al., 2007; Hosseinibalam et al., 2007; Sharaf El Din, 1990; Siddig
214 et al., 2019; Sultan et al., 1995a, 2000). Here we examine intraseasonal variability in the Persian
215 Gulf using satellite data, including altimetry but also gravimetry, and tide gauges.

216 We motivated this study with an exploratory data analysis earlier in the Introduction. We found
217 that roughly half of the monthly ζ variance from altimetry averaged over the Persian Gulf during
218 2002–2015 was concentrated at intraseasonal periods, and that the Persian-Gulf-average altimetric
219 time series of intraseasonal ζ ($\bar{\zeta}$) explained about half of the variance in a composite time series
220 of intraseasonal ζ from coastal tide gauges (Figure 2). These results show that intraseasonal
221 fluctuations contribute importantly to large-scale ζ variability over the Persian Gulf at monthly to
222 decadal periods, and that intraseasonal fluctuations measured locally at the coast largely reflect
223 spatially coherent, basin-wide behavior.

224 To explore intraseasonal ζ in more detail, we apply empirical orthogonal function (EOF) analysis
225 to altimetry data over the Persian Gulf. We identify the spatial structures and temporal behaviors of
226 the orthogonal modes of intraseasonal variability by solving for the eigenvalues and eigenvectors
227 of the covariance matrix of the altimetry data over the Persian Gulf. The eigenvectors correspond
228 to the spatial structures and the eigenvalues indicate the amounts of data variance explained by the
229 various modes. The temporal behaviors of the modes are described by principal-component time
230 series, which are determined by projecting the respective eigenvectors onto the data (von Storch
231 and Zwiers, 1999).

232 The leading mode, which explains 52% of the intraseasonal data variance over the Persian
233 Gulf, is summarized in Figures 3 and 4. It shows a single-signed spatial structure (Figure 3a),
234 indicating basin-wide variation and wholesale raising and lowering of ζ over the Persian Gulf.
235 This is consistent with our earlier finding that the $\bar{\zeta}$ time series from altimetry explains 51% of
236 the variance in the regional composite from tide gauges at intraseasonal timescales (Figure 2).
237 Indeed, this mode's principal-component time series (Figure 4) is perfectly correlated with the $\bar{\zeta}$
238 time series from altimetry (correlation coefficient > 0.99). The leading mode from a complex-
239 valued (Hilbert) EOF analysis explains the same amount of data variance (not shown). This means
240 that out-of-phase relationships between ζ in different parts of the Persian Gulf related to signal
241 propagation are unimportant to this mode, and that this dominant ζ variation reflects an in-phase
242 standing mode of oscillation across the region on these timescales.

243 The spatial structure is also nonuniform (Figure 3a). Magnitudes increase from southeast
244 to northwest across the region, with smaller values (1–3 cm) observed along the United Arab
245 Emirates, Qatar, Bahrain, and southern Iran, and larger values (3–5 cm) apparent off Saudi Arabia,
246 Kuwait, Iraq, and northern Iran. This basin-scale structure could indicate a balance between local
247 wind forcing—strengthening or weakening of the region's prevailing north-northwesterlies—and

248 the combined effects of bottom friction and along-basin pressure gradient. Strongest amplitudes
249 (> 5 cm) are detected off Kuwait and Iraq. Values in this region are highest at the coast and decay
250 offshore. Since depths become shallow and bathymetric gradients weak off Kuwait and Iraq relative
251 to upstream along Iran (Figure 1), these strong amplitudes may indicate coastal-wave amplification
252 related to shoaling and broadening of the topography in this region (e.g., Hughes et al., 2019). It is
253 also possible, as the region is adjacent to the mouths of the Tigris, Euphrates, and Karun rivers, that
254 trapped ζ signals driven by buoyant river discharge also come into play (e.g., Piecuch et al., 2018a).
255 There is also spatial structure in the amount of local data variance explained by this mode: whereas
256 50–80% of local ζ data variance is explained over the interior in the northwestern Persian Gulf,
257 $< 30\%$ is explained in the southwest off Qatar, Bahrain, and the United Arab Emirates (Figure 3b).
258 This suggests important local-scale ζ variability along the southwest coast that is unrelated to the
259 broader-scale behavior resolved by this mode.⁷

260 The ζ response to surface forcing is often described in terms of barotropic (depth-independent)
261 and baroclinic (depth-dependent) adjustments (e.g., Vinogradova et al., 2007). Given the latitude
262 of the Persian Gulf, and the spatiotemporal scales under investigation, basic scaling arguments
263 (Gill and Niiler, 1973; Piecuch et al., 2019) suggest that this mode of ζ variation should be
264 essentially barotropic in nature. For a purely barotropic ocean response, changes in sea level (or
265 subsurface pressure) are mirrored by changes in ocean bottom pressure (Bingham and Hughes,
266 2008; Vinogradova et al., 2007). Hence, if the leading mode of ζ variability from altimetry

⁷Indeed, the second EOF mode (not shown), which explains 8% of the data variance, captures some of the variability in these areas. This mode exhibits amplitudes > 5 cm and explains $> 30\%$ of the data variance off western Qatar, around Bahrain, and along southeastern Saudi Arabia, whereas amplitudes of 2–3 cm and variances explained of 5–30% are apparent in the Southern Shallows off the United Arab Emirates. Since it is tangential to our focus, we do not pay further attention to this mode, other than to posit that—due to the region’s broad, shallow depths (Figure 1)—it may arise from a balance between local winds and bottom friction.

267 (Figure 3, 4) reflects a predominantly barotropic response, then similar R_m variability should be
268 apparent in GRACE.

269 To test this hypothesis, we apply EOF analysis to the GRACE R_m grids over the Persian Gulf.
270 The results are shown in Figures 4 and 5. The leading mode, which explains 88% of the intrasea-
271 sonal GRACE data variance in the Persian Gulf, shows a single-signed spatial pattern, such that
272 variability increases from 1–2 cm in the southeastern Persian Gulf to 3–4 cm in the northwest
273 (Figure 5a). Relatively more local R_m data variance is explained ($> 80\%$) to the north and west,
274 while comparatively less is explained (50–70%) in the southeast (Figure 5b). These patterns from
275 GRACE are qualitatively similar to those from altimetry, but there are quantitative differences
276 (cf. Figures 3, 5). For example, the mode from altimetry exhibits larger amplitudes and richer,
277 more detailed spatial structures than the mode from GRACE (Figures 3a, 5a), whereas the leading
278 GRACE mode explains relatively more data variance compared to the leading altimetry mode
279 (Figures 3b, 5b). These discrepancies probably partly reflect the coarser resolution (and reduced
280 effective spatial degrees of freedom) of GRACE, but could also indicate baroclinic processes or
281 data errors (e.g., residual leakage of terrestrial signals into the GRACE ocean grids).

282 Such differences notwithstanding, results in Figures 3 and 5 suggest that GRACE and altime-
283 try capture facets of the same underlying mode of intraseasonal variation. This suggestion is
284 corroborated by the principal components of the leading EOF modes determined from GRACE
285 and altimetry, which are highly correlated (correlation coefficient of ~ 0.7 ; Figure 4). We also
286 apply maximum covariance analysis (MCA) jointly to altimetry ζ and GRACE R_m data, whereby
287 the eigenvalues and eigenvectors of the cross-covariance matrix between the two data sets are
288 determined (von Storch and Zwiers, 1999). The leading eigenvectors and principal components
289 determined jointly through MCA are identical to those determined separately through EOF anal-
290 ysis, and the gravest MCA mode explains $> 99\%$ of the joint covariance between altimetry and

291 GRACE data (not shown). This suggests that the leading modes of regional ζ and R_m variation are
 292 coupled to one another, and reflect a dominant barotropic response.

293 **4. Forcing mechanisms and ocean dynamics**

294 In the previous section, we established a basin-wide barotropic variation of the Persian Gulf on
 295 intraseasonal timescales. Here we use analytical theory, linear regression, and correlation analysis
 296 to identify the forcing and dynamics responsible for this mode.

297 *a. Linear barotropic model*

298 The leading mode of intraseasonal variability identified previously exhibits higher-order spatial
 299 structure (Figures 3, 5). However, the lowest-order spatial feature is that of a horizontally uniform
 300 fluctuation. For example, the time series of intraseasonal $\bar{\zeta}$ from altimetry explains 93% of the
 301 variance associated with the first altimetric EOF mode (Figures 2–4). Thus, we formulate a linear
 302 model for a horizontally uniform barotropic variation of the Persian Gulf. Our formulation largely
 303 follows Volkov et al. (2016), who use a similar model to consider ζ in the Black Sea. The equations
 304 for conservation of volume within the Persian Gulf and conservation of momentum along the Strait
 305 of Hormuz are

$$306 \quad S\bar{\zeta}_t = S\bar{q} + \frac{S}{\rho g}\bar{p}_t + vWH, \quad (1)$$

$$v_t = -g\zeta_y + \frac{1}{\rho H}\tau - \frac{r}{H}v. \quad (2)$$

307 Here S is surface area of the Persian Gulf, overbar is spatial average over the Persian Gulf, q is
 308 precipitation plus runoff minus evaporation, p is barometric pressure, v is average velocity along
 309 the Strait of Hormuz into the Persian Gulf (positive values increase the volume of the Persian Gulf),
 310 W and H are the width and depth of the Strait of Hormuz, respectively, τ is wind stress along the
 311 Strait of Hormuz (positive in the direction of the Persian Gulf), r is a constant friction coefficient,

312 g is gravity, ρ is seawater density, and subscripts t and y denote partial differentiation in time and
313 the along-strait direction, respectively. Note that, since we express Eqs. (1) and (2) in terms of ζ ,
314 forcing by p appears in the continuity equation rather than in the momentum equation, and takes
315 on a form analogous to the q forcing, such that, as noted by Gill (1982), forcing by a depression
316 of 10 mb would be canceled out by 10 cm of precipitation (cf. also Ponte, 2006). All symbols are
317 described in Table 3 and representative values are given when appropriate.

318 We assume ζ , v , q , p , and τ take wave solutions of the form $\exp(-i\omega t)$ with angular frequency
319 ω and $i \doteq \sqrt{-1}$. Integrating the momentum equation over the length L of the Strait of Hormuz, and
320 rearranging to solve for $\bar{\zeta}$ gives

$$\bar{\zeta} = \left[\zeta_0 + \frac{L}{\rho g H} \tau + \frac{(\lambda - i\omega)}{\sigma^2} \bar{q} - i\omega \frac{(\lambda - i\omega)}{\sigma^2} \frac{\bar{p}}{\rho g} \right] \left/ \left[1 - \frac{\omega^2}{\sigma^2} - i \frac{\lambda \omega}{\sigma^2} \right], \quad (3)$$

321 where ζ_0 represents ζ at the boundary outside the Strait of Hormuz in the Gulf of Oman, and
322 we define $\sigma^2 \doteq WHg/SL$ and $\lambda \doteq r/H$. Physically, $1/\lambda$ is a friction timescale and $1/\sigma$ is a
323 Helmholtz resonance timescale determined by the shape of the Persian Gulf and Strait of Hormuz.
324 (We determine that $1/\sigma \approx 15$ hours, which is small compared to the intraseasonal timescales of
325 interest, so we do not expect a resonant response.) Equivalently, we can write Eq. (3) in the polar
326 complex plane as

$$\bar{\zeta} = z_{\zeta_0} \exp(i\theta_{\zeta_0}) \zeta_0 + z_{\tau} \exp(i\theta_{\tau}) \tau + z_{\bar{q}} \exp(i\theta_{\bar{q}}) \bar{q} + z_{\bar{p}} \exp(i\theta_{\bar{p}}) \bar{p}, \quad (4)$$

327 where

$$\theta_{\zeta_0} \doteq \arctan\left(\frac{\lambda\omega}{\sigma^2 - \omega^2}\right), \quad (5)$$

$$z_{\zeta_0} \doteq \left[\left(1 - \frac{\omega^2}{\sigma^2}\right)^2 + \left(\frac{\lambda\omega}{\sigma^2}\right)^2 \right]^{-1/2}, \quad (6)$$

$$\theta_{\tau} \doteq \arctan\left(\frac{\lambda\omega}{\sigma^2 - \omega^2}\right), \quad (7)$$

$$z_\tau \doteq \left[\left(1 - \frac{\omega^2}{\sigma^2} \right)^2 + \left(\frac{\lambda\omega}{\sigma^2} \right)^2 \right]^{-1/2} \left(\frac{L}{\rho g H} \right), \quad (8)$$

$$\theta_{\bar{q}} \doteq \arctan \left(\frac{\lambda\omega}{\sigma^2} - \frac{\omega}{\lambda} + \frac{\omega^3}{\sigma^2\lambda} \right), \quad (9)$$

$$z_{\bar{q}} \doteq \frac{\lambda}{\sigma^2} \left[1 + \left(\frac{\lambda\omega}{\sigma^2} - \frac{\omega}{\lambda} + \frac{\omega^3}{\sigma^2\lambda} \right)^2 \right]^{1/2} \left[\left(1 - \frac{\omega^2}{\sigma^2} \right)^2 + \left(\frac{\lambda\omega}{\sigma^2} \right)^2 \right]^{-1}, \quad (10)$$

$$\theta_{\bar{p}} \doteq \arctan \left[\left(\frac{\omega}{\lambda} - \frac{\omega^3}{\lambda\sigma^2} - \frac{\omega\lambda}{\sigma^2} \right)^{-1} \right], \quad (11)$$

$$z_{\bar{p}} \doteq \frac{1}{\rho g} \frac{\lambda\omega}{\sigma^2} \left[1 + \left(\frac{\omega}{\lambda} - \frac{\lambda\omega}{\sigma^2} - \frac{\omega^3}{\sigma^2\lambda} \right)^2 \right]^{1/2} \left[\left(1 - \frac{\omega^2}{\sigma^2} \right)^2 + \left(\frac{\omega\lambda}{\sigma^2} \right)^2 \right]^{-1}, \quad (12)$$

In other words, according to Eq. (4), $\bar{\zeta}$ is a linear superposition of the ζ_0 , τ , \bar{q} , and \bar{p} forcing terms, each scaled by an amount z_j and rotated through a phase θ_j , where $j \in \{\zeta_0, \tau, \bar{q}, \bar{p}\}$. We estimate theoretical values for the scaling factors z_j and phase angles θ_j by averaging Eqs. (5)–(12) over the ω range from $2\pi / (6 \text{ months})$ to $2\pi / (2 \text{ months})$ using numerical values for the scalar coefficients λ , σ , L , ρ , g , and H from Table 3. These theoretical values are tabulated in Table 4.

b. Multiple linear regression analysis

To test whether the model described by Eqs. (1)–(12) is informative for understanding observed intraseasonal $\bar{\zeta}$ variability, we perform a multiple linear regression. We model $\bar{\zeta}$ from altimetry as

$$\bar{\zeta} = a_{\zeta_0}\zeta_0 + b_{\zeta_0}\mathcal{H}(\zeta_0) + a_\tau\tau + b_\tau\mathcal{H}(\tau) + a_{\bar{q}}\bar{q} + b_{\bar{q}}\mathcal{H}(\bar{q}) + a_{\bar{p}}\bar{p} + b_{\bar{p}}\mathcal{H}(\bar{p}) + \varepsilon, \quad (13)$$

where \mathcal{H} is the Hilbert transform, the a_j and b_j are real constants, and ε is the residual. We include Hilbert transforms of the various forcings in the regression to allow for possible phase lags between the forcing and the response, as indicated by Eq. (4). We estimate the z_j and θ_j from Eq. (4) from the a_j and b_j in Eq. (13) using properties of Hilbert transforms and trigonometric identities as

$$\theta_j = \arctan(b_j/a_j), \quad (14)$$

$$z_j = \sqrt{a_j^2 + b_j^2}. \quad (15)$$

348 We evaluate Eq. (13) using least squares. For ζ_0 , we use ζ from altimetry averaged over
 349 shallow regions (< 200 m) of the northern Gulf of Oman outside the Strait of Hormuz ($57\text{--}60^\circ\text{E}$,
 350 $25\text{--}28^\circ\text{N}$). For τ , we use along-strait wind stress (315°T) from ERA-Interim averaged over the
 351 Strait of Hormuz ($54\text{--}57.8^\circ\text{E}$, $22.9\text{--}27.4^\circ\text{N}$). For \bar{q} , we use precipitation from GPCP plus river
 352 runoff from JRA55-do minus evaporation from OAFflux averaged over the Persian Gulf ($45\text{--}55^\circ\text{E}$,
 353 $24\text{--}32^\circ\text{N}$). For \bar{p} , we use barometric pressure from ERA-Interim averaged over the Persian Gulf
 354 ($48\text{--}54.8^\circ\text{E}$, $24.4\text{--}29.6^\circ\text{N}$). Uncertainties are estimated using 10 000 iterations of bootstrapping
 355 (Efron and Hastie, 2016).

356 Results of the multiple linear regression are summarized in Figure 6. The regression model
 357 [(13)] explains $70\% \pm 9\%$ (95% confidence interval) of the variance in the $\bar{\zeta}$ data (Figure 6a). This
 358 suggests that Eqs. (1) and (2) represent the dominant physics, and that $\bar{\zeta}$ variability can be largely
 359 understood in terms of local surface forcing by τ , \bar{q} , and \bar{p} and nonlocal boundary forcing by ζ_0 .
 360 In Figure 6b, we break down the relative contributions of the different forcing terms. The primary
 361 driver of $\bar{\zeta}$ is nonlocal forcing by ζ_0 , which explains $50\% \pm 12\%$ of the $\bar{\zeta}$ variance. Local forcing
 362 by τ , \bar{q} , and \bar{p} plays a secondary role. Individually, τ explains $16\% \pm 9\%$, \bar{q} explains $5\% \pm 9\%$,
 363 and \bar{p} explains $10\% \pm 8\%$ of the $\bar{\zeta}$ variance. Surface loading (the combination of \bar{q} and \bar{p} forcing)
 364 explains $14\% \pm 11\%$ of the variance in the data. Collectively, all three local forcing factors taken
 365 together account for $27\% \pm 14\%$ of the $\bar{\zeta}$ variance.⁸

⁸The variance contributions of the individual predictors are not entirely additive, since they are not wholly independent and there is some correlation between them. However, the relative roles of the respective forcings can nevertheless be meaningfully estimated (albeit with uncertainty) because the least-squares problem is generally well posed. After normalizing the predictors to unit variance, the condition number of their covariance matrix is 3.3. This is on the same order as the range of 1.4–2.5 (99% confidence interval) we determine through repeated simulations of four independent random, standard-normal time series (and their Hilbert transforms) with the same length as the observations (not shown).

366 Regression coefficients computed empirically from the data are consistent with values expected
 367 theoretically from first principles (Table 4). For example, the linear regression yields a scaling
 368 factor of $1.5 \pm 0.5 \text{ m Pa}^{-1}$ and a phase angle of 30 ± 25 degrees between τ and $\bar{\zeta}$. This is consistent
 369 with the theoretical ranges of $1.0\text{--}1.3 \text{ m Pa}^{-1}$ and $5\text{--}38$ degrees anticipated from Eqs. (7) and (8).
 370 The regression analysis also suggests a substantial departure from the inverted-barometer response,
 371 manifested in a scaling of $0.8 \pm 0.5 \text{ cm mb}^{-1}$ and a phase of 65 ± 52 degrees between \bar{p} and $\bar{\zeta}$. This
 372 overlaps with the ranges of $0.1\text{--}0.5 \text{ cm mb}^{-1}$ and $56\text{--}87$ degrees expected from Eqs. (11) and (12).
 373 (Recall that the altimeter data have been adjusted for an inverted barometer and that our theory was
 374 developed for ζ , which has the inverted-barometer effect already removed.) This provides evidence
 375 that the results of the multiple linear regression indicate true causal relationships between forcing
 376 and response.

377 Regression results and analytical theory suggest that these relationships can be out of phase, such
 378 that the forcings lead the response by a significant amount (Table 4). To quantify the importance of
 379 out-of-phase behavior, we perform another multiple linear regression analysis, this time omitting
 380 Hilbert transforms and forcing by p from the input [cf. Eq. (13)]. Physically, this alternative
 381 regression model assumes an equilibrium response, and corresponds to the steady state ($\omega \rightarrow 0$)
 382 limit of the governing equations, viz. [cf. Eq. (3)],

$$\bar{\zeta} = \zeta_0 + \frac{L}{\rho g h} \tau + \frac{\lambda}{\sigma^2} \bar{q}. \quad (16)$$

383 This alternate model accounts for slightly less of the $\bar{\zeta}$ data variance ($62\% \pm 10\%$; 95% confidence
 384 interval). This result demonstrates that a majority of the $\bar{\zeta}$ data variance explained by the original
 385 multiple linear regression model [Eq. (13)] is attributable to equilibrium processes and in-phase (or
 386 antiphase) relationships between the forcing and the response, but also that allowing for transient
 387 processes [the time derivatives in Eqs. (1) and (2)] and more general phase relationships between

388 forcing and response leads to a modest, but significant, improvement in terms of explaining $\bar{\zeta}$ data
389 variance.

390 To ascertain whether similar balances are expected at other periods, we consider the $\bar{\zeta}$ response
391 from our model as a function of timescale. We multiply the frequency-dependent scale coefficients
392 [z_j in Eqs. (6), (8), (10), (12)] by a representative fluctuation in the respective forcing [cf. Eq. (4)].
393 We use $|\zeta_0| = 2$ cm, $|\tau| = 0.005$ N m⁻², $|\bar{q}| = 1 \times 10^{-8}$ m s⁻¹, and $|\bar{p}| = 0.5$ hPa based on standard
394 deviations computed from the data. Results are shown in Figure 7. As demanded by Eqs. (6), (8),
395 (10), (12), the $\bar{\zeta}$ responses to ζ_0 , τ , and \bar{q} forcing increase with period, while the $\bar{\zeta}$ adjustment to
396 \bar{p} driving generally decreases with period. The precise rate at which the $\bar{\zeta}$ adjustment approaches
397 its equilibrium response is dictated by friction and the region's shape, as represented by λ and σ .
398 Given the forcing amplitudes, $\bar{\zeta}$ variability is dominated by \bar{p} forcing on timescales of a few days.
399 On timescales of a few days to a few weeks, the influences of \bar{p} , τ , and ζ_0 on $\bar{\zeta}$ can be comparable,
400 depending on the details of friction. At periods longer than a few weeks, forcing by ζ_0 is the
401 primary driver of $\bar{\zeta}$ variability. At all periods, ζ_0 forcing is more influential than τ and \bar{q} forcing.
402 Thus, our findings on intraseasonal timescales are representative of the large-scale, low-frequency
403 barotropic response of the Persian Gulf to external forcing more broadly. This suggests that similar
404 dynamical balances would be obtained in studies of the Persian Gulf over longer timescales. But
405 note that our results are a function of the forcing amplitudes, geometry of the region, and friction.
406 For example, assuming similar friction values and forcing scales, τ and \bar{q} forcing would become
407 relatively more important compared to ζ_0 forcing for a marginal sea with a larger surface area than
408 the Persian Gulf that connects to the open ocean through a strait that is longer, shallower, and
409 narrower than the Strait of Hormuz.

410 *c. Relation to Indian Ocean circulation and climate, and potential predictability*

411 Nonlocal forcing by ζ_0 is the most important contributor to $\bar{\zeta}$ variability (Figures 6b, 7). What
412 is the nature of these fluctuations at the boundary in the Gulf of Oman? How do they relate to
413 larger-scale circulation and climate? To clarify their origin, we compute correlation coefficients
414 between ζ_0 and either ζ or its Hilbert transform $\mathcal{H}(\zeta)$ at every altimetric grid point over the
415 Equatorial and North Indian Ocean. Correlations between ζ_0 and ζ identify regions where ζ is in
416 phase or anti-phase (i.e., 180 degrees out of phase) with ζ_0 , whereas correlations between ζ_0 and
417 $\mathcal{H}(\zeta)$ indicate regions where ζ is in quadrature (90 degrees out of phase) or anti-quadrature (270
418 degrees out of phase) with ζ_0 .

419 In general, ζ_0 is uncorrelated with ζ and $\mathcal{H}(\zeta)$ away from the coast and the equator (Figures 8, 9),
420 suggesting that ζ_0 is unrelated to the dominant ζ variability in these open-ocean regions. However,
421 we observe patterns of significant correlation and anti-correlation along the coast and equator. For
422 example, ζ_0 is correlated with ζ along Pakistan, western India, and Sri Lanka; correlated with $\mathcal{H}(\zeta)$
423 along eastern India, Bangladesh, and Myanmar; correlated with $\mathcal{H}(\zeta)$ and anti-correlated with ζ
424 along Thailand, Malaysia, and Sumatra; and anti-correlated with $\mathcal{H}(\zeta)$ along the western equatorial
425 Indian Ocean between Somalia and the Maldives (Figures 8, 9). Similar correlation patterns are
426 observed between ζ_0 and available tide-gauge data over the Equatorial and North Indian Ocean
427 (Figure 8). Given the gaps in the data, we do not compute Hilbert transforms from the tide-gauge
428 records. [Note also that we computed correlations with altimetry more globally over the ocean,
429 but did not observe large-scale regions of significant correlation between ζ_0 and ζ or $\mathcal{H}(\zeta)$ outside
430 of the Equatorial and North Indian Ocean that suggested viable causal connections (not shown).]

431 These patterns suggest wave propagation along equatorial and coastal waveguides. For example,
432 the correlation between ζ_0 and $\mathcal{H}(\zeta)$ along Bangladesh suggests that ζ_0 lags ζ in this region by 90

433 degrees (one quarter of a period), whereas anti-correlation between ζ_0 and $\mathcal{H}(\zeta)$ in the western
434 equatorial Indian Ocean hints that regional ζ leads ζ_0 by 270 degrees (three quarters of a period).
435 Supposing propagation is eastward along the equator and counterclockwise along the coast (in the
436 Northern Hemisphere), and assuming intraseasonal periods of 60–180 days, we estimate that these
437 phase leads and lags imply propagation speeds of $\sim 1\text{--}3 \text{ m s}^{-1}$. These values are consistent with
438 basic expectations for equatorial waves and coastally trapped waves (e.g., Gill, 1982; Hughes et al.,
439 2019). Indeed, past studies argue that low-latitude wind forcing associated with the Madden-Julian
440 oscillation (MJO) and phases of the monsoon excite wave responses that effect intraseasonal sea-
441 level variability along Sumatra and Java (Iskandar et al., 2005), the Bay of Bengal (Cheng et al.,
442 2013), and India and Sri Lanka (Suresh et al., 2013; Dhage and Strub, 2016). Our results reinforce
443 these past findings, and suggest that these nonlocal forcing effects mediated by large-scale wave
444 responses continue on and are communicated to the Persian Gulf.

445 We perform a similar analysis with GRACE data. Correlations between ζ_0 and either GRACE
446 R_m or its Hilbert transform $\mathcal{H}(R_m)$ over the Indian Ocean are shown in Figure 10. While there
447 is essentially no meaningful correlation anywhere between ζ_0 and $\mathcal{H}(R_m)$, there is significant
448 correlation between ζ_0 and GRACE R_m broadly over much of the Indian Ocean (Figure 10). This
449 suggests that ζ_0 is also related to a basin-scale equilibrium response in addition to the more transient
450 wave adjustments trapped to the coast and the equator suggested by the altimetry data (Figures 8, 9).
451 Indeed, the correlation pattern between ζ_0 and R_m (Figure 10a) is similar to the spatial structure
452 of the intraseasonal fluctuation of the Indian Ocean identified by Rohith et al. (2019) based on
453 data from bottom-pressure recorders, GRACE, and a general circulation model. They argue that
454 wind-curl fluctuations at 30–80-day periods over the Wharton basin associated with the MJO excite
455 planetary and topographic Rossby wave responses that lead to a basin-wide barotropic variation
456 that is confined to the Indian Ocean by bathymetric contours. Our results provide observational

457 evidence that this large-scale intraseasonal fluctuation affects variability not only over the deep
458 Indian Ocean but also within its shallow marginal seas.

459 Wave propagation apparent in Figures 8 and 9 hints that ζ_0 variability may be predictable to some
460 extent. That is, armed with upstream ζ information, it may be possible to anticipate ζ_0 variance in
461 advance. To test this possibility, we compute lagged correlation coefficients between ζ_0 and ζ at
462 earlier times over the Equatorial and North Indian Ocean. Results are shown in Figures 11 and 12
463 for lead times of 1 and 2 months, respectively. Considering a 1-month lead time, we find positive
464 correlations between ζ_0 and ζ upstream along the Indian Subcontinent and Maritime Continent,
465 from eastern India to Sumatra, and negative correlations over the western Equatorial Indian Ocean
466 between Somalia and the Maldives (Figure 11). Indeed, the pattern of correlation between ζ_0 and
467 ζ 1 month earlier is similar to the structure of correlation between ζ_0 and $\mathcal{H}(\zeta)$ (cf. Figures 9, 11),
468 suggesting a dominant timescale of ~ 4 months. Values of 0.4–0.5 are apparent off Myanmar and
469 Sumatra (Figure 11), hinting that 16–25% of the variance in ζ_0 can be predicted from ζ knowledge
470 in these regions 1 month earlier. Considering a lead time of 2 months, we observe that ζ_0 and ζ
471 are largely uncorrelated, except for along Pakistan, western India, and Sri Lanka, where negative
472 coefficients between -0.3 and -0.4 are seen. This implies that 9–16% of the ζ_0 variance can be
473 predicted from ζ observations along this coastline 2 months earlier. Considering lead times of 3
474 months and longer, we detect no significant correlations between ζ_0 and ζ elsewhere (not shown),
475 indicating that there is little skill in predictions of intraseasonal ζ_0 variability more than 2 months
476 into the future from wave characteristics and ocean memory alone. Considering the available
477 tide-gauge records in the Equatorial and North Indian Ocean, we obtain similar patterns of lagged
478 correlations (Figures 11, 12).

5. Summary and discussion

We studied intraseasonal variability in ocean dynamic sea level (ζ) over the Persian Gulf during 2002–2015 using satellite observations and other data (Figures 1, 2). Intraseasonal ζ variability in the Persian Gulf manifests in a basin-wide, vertically coherent mode of fluctuation (Figures 3–5). This large-scale mode is related to freshwater flux and barometric pressure over the Persian Gulf, wind stress along the Strait of Hormuz, and nonlocal forcing embodied in ζ variations at the boundary in the Gulf of Oman (Figures 6, 7). The ζ boundary condition shows rich correlation patterns with altimetry data upstream along the Indian Subcontinent, Maritime Continent, and equatorial Indian Ocean (Figures 8, 9), and with GRACE data broadly over the Indian Ocean (Figure 10), suggesting an intimate connection between intraseasonal ζ variability in the Persian Gulf and large-scale circulation and climate in the Equatorial and North Indian Ocean mediated by equatorial-, Rossby-, and coastal-wave processes identified previously (Cheng et al., 2013; Dhage and Strub, 2016; Iskandar et al., 2005; Oliver and Thompson, 2010; Rohith et al., 2019; Suresh et al., 2013, 2016; Waliser et al., 2003, 2004). Our results indicate that some intraseasonal ζ variance in the Persian Gulf may be predictable a month or so in advance from upstream observations and the physics of coastal wave propagation and ocean memory (Figures 11, 12).

Our results establish the dominant magnitudes, scales, and mechanisms of intraseasonal sea-level variability in the Persian Gulf, and thus build on findings from past works that emphasize seasonal cycles and decadal trends (Al-Subhi, 2010; Alothman et al., 2014; Ayhan, 2020; El-Gindy, 1991; El-Gindy and Eid, 1997; Hassanzadeh et al., 2007; Hosseinibalam et al., 2007; Sharaf El Din, 1990; Siddig et al., 2019; Sultan et al., 1995a, 2000). Our study demonstrates that GRACE satellite retrievals are informative for interrogating coastal sea level over a semi-enclosed marginal sea, thereby complementing previous efforts that demonstrate the value of GRACE data in other

502 marginal seas (Feng et al., 2012, 2014; Fenoglio-Marc et al., 2006, 2012; Landerer and Volkov,
503 2013; Loomis and Luthcke, 2017; Piecuch and Ponte, 2015; Piecuch et al., 2018b; Tregoning et
504 al., 2008; Wahr et al., 2014; Wang et al., 2015; Wouters and Chambers, 2010), and encouraging
505 further exploration of GRACE data in the Persian Gulf at other timescales.

506 Intraseasonal ζ variability in the Persian Gulf is coupled to variable volume exchanges between
507 the Persian Gulf and Arabian Sea through the Strait of Hormuz. Observations of the time-variable
508 transport through the Strait of Hormuz are limited to short field campaigns (e.g., Johns et al., 2003).
509 Therefore, it is informative to consider the transport variability implied by data here and permitted
510 by our model. Based on volume conservation [Eq. (1)], we make a rough estimate of the variable
511 transport using our time series of surface freshwater flux and time derivatives of ζ and air pressure
512 (not shown). The standard deviation of the transport estimate is $2.7 \times 10^3 \text{ m}^3 \text{ s}^{-1}$. In relative terms,
513 this represents a departure of 19–28% from the steady state transport required to balance canonical
514 values for the average evaporation over the Persian Gulf of $1.4\text{--}2 \text{ m y}^{-1}$ (Privett, 1959; Ahmad and
515 Sultan, 1990; Johns et al., 2003). These transport fluctuations arise from subtle velocity variations
516 averaged over the width and depth of the Strait of Hormuz of only $\sim 0.9 \text{ mm s}^{-1}$. An interrogation
517 of our model equations [Eqs. (1) and (2)] suggests that these variations in transport result mainly
518 from a combination of local surface freshwater flux and nonlocal forcing at the boundary over the
519 Gulf of Oman (see Appendix).

520 This investigation advances knowledge of sea-level variability in the Persian Gulf. It also paves
521 the way for future studies, pointing to open questions. For example, we developed and tested a
522 theory for a horizontally uniform fluctuation of the Persian Gulf. However, the leading mode of
523 intraseasonal ζ variability in the region exhibits spatial structure, such that magnitudes are larger in
524 the northwest and smaller in the southeast of the Persian Gulf (Figures 3, 5). We hypothesized that
525 this spatial structure could arise from local surface forcing or topographic effects on coastal-wave

526 propagation. Future studies based on high-resolution ocean models should test these hypotheses
527 and identify the controls on spatial structure.

528 It also remains to quantify whether baroclinic effects and steric processes contribute to the
529 dominant intraseasonal ζ variability in the Persian Gulf. Vertical density stratification in the region
530 is stronger during summer than during winter (Reynolds, 1993), and offshore bathymetric gradients
531 are more dramatic to the east along Iran than to the north, west, and south along other Persian-Gulf
532 nations (Figure 1). Coastal wave theory (Hughes et al., 2019, and references therein) suggests that
533 such conditions favor barotropic (topographic) wave ζ adjustment in wintertime or along the coast
534 from Iraq to Oman, but that baroclinic (Kelvin) wave ζ response may be relevant along the coast
535 of Iran in summertime. Local surface heat fluxes could also effect important variations in density
536 and steric height. For example, fluctuations in evaporation of $\pm 1 \times 10^{-8} \text{ m s}^{-1}$ (cf. Figures 6, 7)
537 correspond to variations in latent heat flux of $\pm 25 \text{ W m}^{-2}$ [see Eq. (4a) in Large and Yeager, 2004],
538 which, if sustained for periods of 60–180 d, would result in fluctuations in steric height of 2–5 mm
539 [see Eq. (8) in Vivier et al., 1999]. Steric changes were not estimated due to the lack of continuous
540 hydrographic records in the Persian Gulf (e.g., Good et al., 2013). However, future studies could
541 explore this topic by comparing differences between altimetry and GRACE, which are potentially
542 informative of steric processes, to sea-level changes anticipated from the passive response to local
543 surface heat flux (e.g., Cabanes et al., 2006), or sea-surface temperature data assuming that ocean
544 temperature variations are vertically coherent (e.g., Meyssignac et al., 2017).

545 We determined that dynamic response to barometric pressure and freshwater flux is a secondary
546 but nevertheless significant contributor to intraseasonal ζ variability in the Persian Gulf (Figure 6).
547 This is interesting, given that the barotropic ocean response to surface loading is generally expected
548 to be isostatic on timescales longer than a few days (e.g., Wunsch and Stammer, 1997; Ponte, 2006).
549 In our model physics, the dynamic response is permitted by friction through the Strait of Hormuz.

550 Our finding that freshwater flux elicits a ζ response on the order of a few mm (Figure 6) is consistent
551 with the basic ζ magnitudes simulated for this region across subdaily to annual timescales by Ponte
552 (2006) using a 1-year simulation from a global barotropic ocean general circulation model forced
553 with evaporation and precipitation (Hirose et al., 2001); however, that model was designed for
554 global studies, and it used coarse resolution ($\sim 1^\circ$) and a large friction coefficient ($2 \times 10^{-2} \text{ m s}^{-1}$),
555 which may not accurately capture important physics in and around the Persian Gulf. Future studies
556 using high-resolution ocean models would be informative for clarifying the nature of intraseasonal
557 ζ variation in the Persian Gulf and the role of surface loading. Also relevant here is the fact that the
558 non-isostatic response to barometric pressure is roughly in quadrature with the forcing (Table 4).
559 This highlights the importance of considering phase information when testing for departures from
560 a pure inverted-barometer response in sea-level data (e.g., Mathers and Woodworth, 2001, 2004).

561 Past studies argue that low-latitude wind forcing of the Indian Ocean related to large-scale
562 climate modes excites wave responses that effect intraseasonal sea-level variability along the Indian
563 Subcontinent and Maritime Continent, from Sumatra to western India (Cheng et al., 2013; Dhage
564 and Strub, 2016; Iskandar et al., 2005; Suresh et al., 2013). We provide evidence that these coastal-
565 trapped waves continue propagating downstream and influence sea level in the Gulf of Oman and
566 Persian Gulf (Figures 8, 9). We acknowledge that, while they suggest wave propagation, Figures 8
567 and 9 could alternatively indicate the spatial scales of the atmospheric forcing. For example,
568 large-scale wind forcing along the equator and off the southern tip of the Indian subcontinent could
569 simultaneously excite equatorial waves and coastal waves propagating in the cyclonic sense along
570 the west coast of the Indian subcontinent (e.g., Suresh et al., 2013; Dhage and Strub, 2016). Future
571 studies should identify the dominant centers of action of atmospheric forcing of intraseasonal ζ
572 variability in the Persian Gulf, and whether coastal-trapped waves arriving in the Gulf of Oman
573 have their origin in equatorial waves that impinged on the Maritime Continent. Our results also

574 raise questions of whether such wave signals are felt even farther downstream along the coastal
575 waveguide, for example, in the Red Sea. Previous investigations of sea-level variability in the
576 Red Sea on timescales from days to decades largely emphasize the role of more local forcing
577 (Abdelrahman, 1997; Churchill et al., 2018; Cromwell and Smeed, 1998; Osman, 1984; Patzert,
578 1974; Sofianos and Johns, 2001; Sultan and Elghribi 2003; Sultan et al., 1995b, 1995c, 1996).
579 However, recent work by Alawad et al. (2017, 2019) suggests that mean sea-level variability in the
580 Red Sea is partly related to large-scale modes of climate variability. These authors reason that this
581 relationship is mediated by westward propagation of off-equatorial Rossby waves originating in the
582 eastern tropical Indian Ocean. Based on our results, we hypothesize that coastal-wave propagation
583 may also play a role in facilitating this relationship between sea level in the Red Sea and large-scale
584 climate. We leave it to future studies to test this hypothesis.

585 *Acknowledgments.* The authors acknowledge support from NASA through the Sea Level Change
586 Team (grant 80NSSC20K1241) and GRACE Follow-On Science Team (grant 80NSSC20K0728).
587 The authors appreciate comments from two anonymous reviewers that improved the manuscript.

588 *Data availability statement.* Data are available through links provided in Table 1. Matlab codes
589 used for processing the data and producing the results are available from the corresponding author
590 upon request.

591 APPENDIX

592 **Transport variation through the Strait of Hormuz**

593 Insights onto the local and nonlocal forcing of transport variability through the Strait of Hormuz
594 are given by our model. Substituting Eq. (3) for $\bar{\zeta}_t$ in Eq. (1), and assuming plane-wave solutions,

595 we obtain after rearranging and collecting terms,

$$vWH = -i\omega S \left[\zeta_0 + \frac{L}{\rho g H} \tau - \frac{i}{\omega} \bar{q} - \frac{\bar{p}}{\rho g} \right] \left/ \left[1 - \frac{\omega^2}{\sigma^2} - i \frac{\lambda \omega}{\sigma^2} \right] \right., \quad (\text{A1})$$

596 or, equivalently,

$$vWH = \tilde{z}_{\zeta_0} \exp(i\tilde{\theta}_{\zeta_0}) \zeta_0 + \tilde{z}_{\tau} \exp(i\tilde{\theta}_{\tau}) \tau + \tilde{z}_{\bar{q}} \exp(i\tilde{\theta}_{\bar{q}}) \bar{q} + \tilde{z}_{\bar{p}} \exp(i\tilde{\theta}_{\bar{p}}) \bar{p}, \quad (\text{A2})$$

597 where

$$\tilde{\theta}_{\zeta_0} \doteq \arctan \left(\frac{\omega^2 - \sigma^2}{\lambda \omega} \right), \quad (\text{A3})$$

$$\tilde{z}_{\zeta_0} \doteq \omega S \left[\left(1 - \frac{\omega^2}{\sigma^2} \right)^2 + \left(\frac{\lambda \omega}{\sigma^2} \right)^2 \right]^{-1/2}, \quad (\text{A4})$$

$$\tilde{\theta}_{\tau} \doteq \arctan \left(\frac{\omega^2 - \sigma^2}{\lambda \omega} \right), \quad (\text{A5})$$

$$\tilde{z}_{\tau} \doteq \omega S \left[\left(1 - \frac{\omega^2}{\sigma^2} \right)^2 + \left(\frac{\lambda \omega}{\sigma^2} \right)^2 \right]^{-1/2} \left(\frac{L}{\rho g H} \right), \quad (\text{A6})$$

$$\tilde{\theta}_{\bar{q}} \doteq \arctan \left(\frac{\lambda \omega}{\sigma^2 - \omega^2} \right), \quad (\text{A7})$$

$$\tilde{z}_{\bar{q}} \doteq S \left[\left(1 - \frac{\omega^2}{\sigma^2} \right)^2 + \left(\frac{\lambda \omega}{\sigma^2} \right)^2 \right]^{-1/2}, \quad (\text{A8})$$

$$\tilde{\theta}_{\bar{p}} \doteq \arctan \left(\frac{\omega^2 - \sigma^2}{\lambda \omega} \right), \quad (\text{A9})$$

$$\tilde{z}_{\bar{p}} \doteq \frac{\omega S}{\rho g} \left[\left(1 - \frac{\omega^2}{\sigma^2} \right)^2 + \left(\frac{\lambda \omega}{\sigma^2} \right)^2 \right]^{-1/2}. \quad (\text{A10})$$

605 To quantify the relative roles of the different surface and boundary forcing terms on transport
 606 as a function of timescale, we multiply the frequency-dependent scaling coefficients [\tilde{z}_j in Eqs.
 607 (A4), (A6), (A8), (A10)] by the same forcing fluctuations that we used earlier in section 4.b and
 608 Figure 7 ($|\zeta_0| = 2$ cm, $|\tau| = 0.005$ N m⁻², $|\bar{q}| = 1 \times 10^{-8}$ m s⁻¹, $|\bar{p}| = 0.5$ hPa). Results are shown
 609 in Figure A1. Resonant responses to ζ_0 , τ , and \bar{p} are seen near the Helmholtz period $2\pi/\sigma \sim 4$ d,
 610 when maximum values ($\sigma^2 S |\zeta_0| / \lambda$, $\sigma^2 S L |\tau| / \lambda \rho g H$, and $\sigma^2 S |\bar{p}| / \lambda \rho g$, respectively) are achieved.

611 At periods shorter (longer) than $2\pi/\sigma$, the transport response to ζ_0 , τ , and \bar{p} grows (decays) with
612 period, such that $vWH \rightarrow 0$ as $\omega \rightarrow 0$. In contrast, the transport response to \bar{q} increases universally
613 with period, approaching the asymptotic limit $vWH \rightarrow S\bar{q}$ as $\omega \rightarrow 0$.

614 Given the amplitudes of the forcings, transport variations are predominantly driven by ζ_0 and \bar{q}
615 on intraseasonal timescales. At longer timescales, forcing by \bar{q} dominates, whereas ζ_0 , τ , and \bar{p} are
616 more important drivers at shorter timescales. At all timescales, transport variations owing to local
617 τ and \bar{p} forcing are $\sim 1/3$ and $\sim 1/4$ as large, respectively, as transport variations due to nonlocal
618 ζ_0 forcing. This analytical exercise suggests that the intraseasonal transport variations through the
619 Strait of Hormuz, estimated in the Discussion, mainly reflect a combination of local \bar{q} and nonlocal
620 ζ_0 forcing effects.

621 As discussed earlier, these results are a function of the forcing scales, details of friction, and the
622 geometry of the region, and the various forcings could be more or less important if these parameters
623 were different (e.g., for a different marginal sea).

624 **References**

- 625 Abdelrahman, S. M., 1997: Seasonal Fluctuations of Mean Sea Level at Gizan, Red Sea. *Journal*
626 *of Coastal Research*, 13(4), 1166–1172,
- 627 Ablain, M., A. Cazenave, G. Larnicol, M. Balmaseda, P. Cipollini, Y. Faugère, M. J. Fernandes,
628 O. Henry, J. A. Johannessen, P. Knudsen, O. Andersen, J. Legeais, B. Meyssignac, N. Picot,
629 M. Roca, S. Rudenko, M. G. Scharffenberg, D. Stammer, G. Timms, and J. Benveniste, 2015:
630 Improved sea level record over the satellite altimetry era (1993–2010) from the Climate Change
631 Initiative project. *Ocean Science*, 11, 67–82, <https://doi.org/10.5194/os-11-67-2015>.

- 632 Adhikari, S., E. R. Ivins, T. Frederikse, F. W. Landerer, and L. Caron, 2019: Sea-level fin-
633 gerprints emergent from GRACE mission data. *Earth System Science Data*, 11, 629–646,
634 <https://doi.org/10.5194/essd-11-629-2019>.
- 635 Adler, R. F., G. J. Huffman, A. Chang, R. Ferraro, P. Xie, J. Janowiak, B. Rudolf, U.
636 Schneider, S. Curtis, D. Bolvin, A. Gruber, J. Susskind, and P. Arkin, 2003: The Ver-
637 sion 2 Global Precipitation Climatology Project (GPCP) Monthly Precipitation Analysis
638 (1979-Present). *Journal of Hydrometeorology*, 4,1147–1167, [https://doi.org/10.1175/1525-7541\(2003\)004<1147:TVGPCP>2.0.CO;2](https://doi.org/10.1175/1525-7541(2003)004<1147:TVGPCP>2.0.CO;2)
- 640 Ahmad, F., and S. A. R. Sultan, 1991: Annual mean surface heat fluxes in the Arabian Gulf
641 and the net heat transport through the Strait of Hormuz. *Atmosphere-Ocean*, 29(1), 54–61,
642 <https://doi.org/10.1080/07055900.1991.9649392>
- 643 al-Chalabi, I., 2007: Oil. The Geopolitics of Oil and Iraq. *New England Journal of Public Policy*,
644 21(2), 136–139, <https://scholarworks.umb.edu/nejpp/vol21/iss2/13>.
- 645 Al-Jeneid, S., Bahnassy, M., Nasr, S., and El Raey, M., 2008: Vulnerability assessment and
646 adaptation to the impacts of sea level rise on the Kingdom of Bahrain. *Mitigation and Adaptation*
647 *Strategies for Global Change*, 13, 87–104, <https://doi.org/10.1007/s11027-007-9083-8>.
- 648 Al-Subhi, A. M., 2010: Tide and sea level characteristics at Juaymah, west coast of the
649 Arabian Gulf. *Journal of King Abdulaziz University Marine Science*, 21(1), 133–149,
650 <https://doi.org/10.4197/mar.21-1.8>.
- 651 Alawad, K. a. I., A. M. Al-Subhi, M. A. Alsaafani, and T. M. Alraddadi, 2017: Signatures of
652 Tropical climate modes on the Red Sea and Gulf of Aden Sea Level. *Indian Journal of Geo*
653 *Marine Sciences*, 46(10), 2088–2096, <http://nopr.niscair.res.in/handle/123456789/42751>.

- 654 Alawad, K. a. I., A. M. Al-Subhi, M. A. Alsaafani, M. Ionita, and G. Lohmann, 2019: Large-Scale
655 Mode Impacts on the Sea Level over the Red Sea and Gulf of Aden. *Remote Sensing*, *11*, 2244,
656 <https://doi.org/10.3390/rs11192224>.
- 657 Alothman, A. O., M. S. Bos, R. M. S. Fernandes, and M. E. Ayhan, 2014: Sea level
658 rise in the north-western part of the Arabian Gulf. *Journal of Geodynamics*, *81*, 105–110,
659 <https://doi.org/10.1016/j.jog.2014.09.002>.
- 660 Amin, A., and K. Bankher, 1997: Causes of land subsidence in the Kingdom of Saudi Arabia.
661 *Natural Hazards*, *16*(1), 57–63, <https://doi.org/10.1023/A:1007942021332>.
- 662 Ayhan, M. E., 2020: Dynamic harmonic regression modeling for monthly mean sea levels at tide
663 gauges within the Arabian Gulf. *Journal of Geodesy*, *94*(46), [https://doi.org/10.1007/s00190-](https://doi.org/10.1007/s00190-020-01371-x)
664 [020-01371-x](https://doi.org/10.1007/s00190-020-01371-x).
- 665 Barnes, J., and A. M. Jaffe, 2006: The Persian Gulf and the Geopolitics of Oil. *Survival: Global*
666 *Politics and Strategy*, *48*(1), 143–162, <https://doi.org/10.1080/00396330600594348>.
- 667 Barzandeh, A., N. Eshghi, F. Hosseinibalam, and S. Hassanzadeh, 2018: Wind-driven coastal
668 upwelling along the northern shoreline of the Persian Gulf. *Bollettino di Geofisica Teorica ed*
669 *Applicata*, *59*(3), 301–302, <https://doi.org/10.4430/bgta0235>.
- 670 Bingham, R. J., and C. W. Hughes, 2008: The relationship between sea-level and bottom pressure
671 variability in an eddy permitting ocean model. *Geophysical Research Letters*, *35*, L03602,
672 <https://doi.org/10.1029/2007GL032662>.
- 673 Burgos, A. G., B. D. Hamlington, P. R. Thompson, and R. D. Ray: Future Nuisance Flooding
674 in Norfolk, VA, From Astronomical Tides and Annual to Decadal Internal Climate Variability.
675 *Geophysical Research Letters*, *45*, 12432–12439, <https://doi.org/10.1029/2018GL079572>.

- 676 Cabanes, C., T. Huck, and A. Colin de Verdière, 2006: Contributions of Wind Forcing and
677 Surface Heating to Interannual Sea Level Variations in the Atlantic Ocean. *Journal of Physical*
678 *Oceanography*, 36, 1739–1750.
- 679 Carrère, L., and F. Lyard, 2003: Modeling the barotropic response of the global ocean to at-
680 mospheric wind and pressure forcing—comparisons with observations. *Geophysical Research*
681 *Letters*, 30(6), 1275, <https://doi.org/10.1029/2002GL016473>.
- 682 Carrère, L., Y. Faugère, and M. Ablain, 2016: Major improvement of altimetry sea level estima-
683 tions using pressure-derived corrections based on ERA-Interim atmospheric reanalysis. *Ocean*
684 *Science*, 12, 825–842, <https://doi.org/10.5194/os-12-825-2016>.
- 685 Chao, S.-Y., T. W. Kao, and K. R. Al-Hajri, 1992: A numerical investigation of the cir-
686 culation in the Arabian Gulf. *Journal of Geophysical Research*, 97(C7), 11219–11236.
687 <https://doi.org/10.1029/92JC00841>.
- 688 Cheng, X., S.-P. Xie, J. P. McCreary, Y. Qi, Y., and Y. Du, 2013: Intraseasonal variability of sea
689 surface height in the Bay of Bengal. *Journal of Geophysical Research Oceans*, 118(2), 816–430,
690 <https://doi.org/10.1002/jgrc.20075>.
- 691 Churchill, J. H., Abualnaja, Y., Limeburner, R., and Nellayaputhenpeedika, M., 2018: The dynam-
692 ics of weather-band sea level variations in the Red Sea. *Regional Studies in Marine Science*, 24,
693 336–342, <https://doi.org/10.1016/j.rsma.2018.09.006>.
- 694 Cromwell, D., and Smeed, D. A., 1998: Altimetric observations of sea level cycles near
695 the Strait of Bab al Mandab. *International Journal of Remote Sensing*, 19(8), 1561–1578,
696 <https://doi.org/10.1080/014311698215351>.

- 697 Dangendorf, S., A. Arns, J. G. Pinto, P. Ludwig, and J. Jensen, 2016: The exceptional influence of
698 storm ‘Xaver’ on design water levels in the German Bight. *Environmental Research Letters*, *11*,
699 054001, <https://doi.org/10.1088/1748-9326/11/5/054001>.
- 700 Dangendorf, S., C. Hay, F. M. Calafat, M. Marcos, C. G. Piecuch, K. Berk, and J. Jensen, 2019:
701 Persistent acceleration in global sea-level rise since the 1960s. *Nature Climate Change*, *9*,
702 705–710, <https://doi.org/10.1038/s41558-019-0531-8>.
- 703 Dee, D. P., S. M. Uppala, A. J. Simmons, P. Berrisford, P. Poli, S. Kobayashi, U. Andrae, M. A.
704 Balmaseda, G. Balsamo, P. Bauer, P. Bechtold, A. C. M. Beljaars, L. van de Berg, J. Bidlot,
705 N. Bormann, C. Delsol, R. Dragani, M. Fuentes, A. J. Geer, L. Haimberger, S. B. Healy, H.
706 Hersbach, E. V. Hólm, L. Isaksen, P. Kållberg, M. Köhler, M. Matricardi, A. P. McNally, B. M.
707 Monge-Sanz, J.-J. Morcrette, B.-K. Park, C. Peubey, P. de Rosnay, C. Tavolato, J.-N. Thépaut,
708 and F. Vitart, 2011: The ERA-Interim reanalysis: configuration and performance of the data
709 assimilation system. *Quarterly Journal of the Royal Meteorological Society*, **137**, 553–597,
710 <https://doi.org/10.1002/qj.828>.
- 711 Dhage, L., and P. T. Strub, 2016: Intra-seasonal sea level variability along the
712 west coast of India. *Journal of Geophysical Research Oceans*, *121*, 8172–8188,
713 <https://doi.org/10.1002/2016JC011904>.
- 714 Efron, B., and T. Hastie, 2016: *Computer Age Statistical Inference: Algorithms, Evidence, and*
715 *Data Science*, Cambridge University Press, 495 pp.
- 716 El-Gindy, A. A. H., 1991: Sea level variations and their relations to the meteorological factors in
717 the Arab Gulf area with stress on monthly means. *International Hydrographic Review*, *68*(1),
718 109–125.

- 719 El-Gindy, A. A., and F. M. Eid, 1997: The seasonal variations of sea level due to density variations
720 in the Arabian Gulf and Gulf of Oman. *Pakistan Journal of Marine Sciences*, 6(1–2), 1–12.
- 721 Emery, K. O., 1956: Sediments and water in the Persian Gulf. *Bulletin of the American Association*
722 *of Petroleum Geologists*, 40(10), 2354–2383, [https://doi.org/10.1306/5CEAE595-16BB-11D7-](https://doi.org/10.1306/5CEAE595-16BB-11D7-8645000102C1865D)
723 8645000102C1865D.
- 724 Feng, W., M. Zhong, and H. Z. Xu, 2012: Sea level variations in the South China Sea inferred
725 from satellite gravimetry, altimetry, and oceanographic data. *Science in China Series D*, 55, 10,
726 1696–1701, <https://doi.org/10.1007/s11430-012-4394-3>.
- 727 Feng, W., J.-M. Lemoine, M. Zhong, M., and H. T. Hsu, 2014: Mass-induced sea
728 level variations in the Red Sea from GRACE, steric-corrected altimetry, in situ bot-
729 tom pressure records, and hydrographic observations. *Journal of Geodynamics*, 78, 1–7.
730 <http://dx.doi.org/10.1016/j.jog.2014.04.008>.
- 731 Fenoglio-Marc, L., J. Kusche, and M. Becker, 2006: Mass variation in the Mediterranean Sea
732 from GRACE and its validation by altimetry, steric and hydrologic fields. *Geophysical Research*
733 *Letters*, 33(L19606), <https://doi.org/10.1029/2006GL026851>.
- 734 Fenoglio-Marc, L., R. Rietbroek, S. Grayek, M. Becker, J. Kusche, and E. Stanev, 2012: Wa-
735 ter mass variation in the Mediterranean and Black Seas. *Journal of Geodynamics*, 59–60,
736 <https://doi.org/10.1016/j.jog.2012.04.001>.
- 737 Frederikse, T., F. Landerer, L. Caron, S. Adhikari, D. Parkes, V. W. Humphrey, S. Dangendorf, P.
738 Hogarth, L. Zanna, L. Cheng, and Y.-H. Wu: The causes of sea-level rise since 1900. *Nature*,
739 584, 393–397, <https://doi.org/10.1038/s41586-020-2591-3>.
- 740 Gill, A. E., 1982: *Atmosphere-Ocean Dynamics*, Academic Press, 680 pp.

- 741 Gill, A. E., and P. P. Niiler, 1973: The theory of the seasonal variability in the ocean. *Deep-Sea*
742 *Research*, 20, 141–177, [https://doi.org/10.1016/0011-7471\(73\)90049-1](https://doi.org/10.1016/0011-7471(73)90049-1).
- 743 Good, S. A., M. J. Martin, and N. A. Rayner, 2013: EN4: Quality controlled ocean temperature
744 and salinity profiles and monthly objective analyses with uncertainty estimates. *Journal of*
745 *Geophysical Research*, 118, 6704–6716, <https://doi.org/10.1002/2013JC009067>.
- 746 Gregory, J. M., S. M. Griffies, C. W. Hughes, J. A. Lowe, J. A. Church, I. Fukumori, N. Gomez,
747 R. E. Kopp, F. Landerer, G. Le Cozannet, R. M. Ponte, D. Stammer, M. E. Tamisiea, and R. S.
748 W. van de Wal, 2019: Concepts and Terminology for Sea Level: Mean, Variability and Change,
749 Both Local and Global. *Surveys in Geophysics*, 40, 1251–1289, [https://doi.org/10.1007/s10712-](https://doi.org/10.1007/s10712-019-09525-z)
750 [019-09525-z](https://doi.org/10.1007/s10712-019-09525-z).
- 751 Hassanzadeh, S., A. Kiasatpour, and F. Hosseinibalam, 2007: Sea-level response to atmospheric
752 forcing along the north coast of Persian Gulf. *Meteorology and Atmospheric Physics*, 95, 223–
753 237, <https://doi.org/10.1007/s00703-006-0213-8>.
- 754 Hirose, N., I. Fukumori, V. Zlotnicki, and R. M. Ponte, 2001: Modeling the high-
755 frequency barotropic response of the ocean to atmospheric disturbances: Sensitivity to forc-
756 ing, topography, and friction. *Journal of Geophysical Research*, 106(C12), 30987–30995,
757 <https://doi.org/10.1029/2000JC000763>.
- 758 Holgate, S. J., A. Matthews, P. L. Woodworth, L. J. Rickards, M. E. Tamisiea, E. Bradshaw, P.
759 R. Foden, K. M. Gordon, S. Jevrejeva, and J. Pugh, 2013: New Data Systems and Products
760 and the Permanent Service for Mean Sea Level. *Journal of Coastal Research*, 29(3), 493–504,
761 <https://doi.org/10.2112/JCOASTRES-D-12-00175.1>.

- 762 Hosseinibalam, F., S. Hassanzadeh, and A. Kiasatpour, 2007: Interannual variability and seasonal
763 contribution of thermal expansion to sea level in the Persian Gulf. *Deep-Sea Research Part I*,
764 54, 1474–1485, <https://doi.org/10.1016/j.dsr.2007.05.005>.
- 765 Hughes, C. W., I. Fukumori, S. M. Griffies, J. M. Huthnance, S. Minobe, P. Spence, K. R.
766 Thompson, and A. Wise, 2019: Sea Level and the Role of Coastal Trapped Waves in Medi-
767 ating the Influence of the Open Ocean on the Coast. *Surveys in Geophysics*, 40, 1467–1492,
768 <https://doi.org/10.1007/s10712-019-09535-x>.
- 769 Iskandar, I., W. Mardiansyah, Y. Masumoto, and T. Yamagata, 2005: Intraseasonal Kelvin waves
770 along the southern coast of Sumatra and Java. *Journal of Geophysical Research*, 110(C04013),
771 <https://doi.org/10.1029/2004JC002508>.
- 772 Johns, W. E., G. A. Jacobs, J. C. Kindle, S. P. Murray, and M. Carron, 1999: Arabian Marginal
773 Seas and Gulfs: report of a workshop held at Stennis Space Center, Miss., 11–13 May 1999.
774 University of Miami RSMAS Technical Report 2000-01, 60 pp.
- 775 Johns, W. E., F. Yao, D. B. Olson, S. A. Josey, J. P. Grist, and D. A. Smeed, 2003: Ob-
776 servations of seasonal exchange through the Straits of Hormuz and the inferred heat and
777 freshwater budgets of the Persian Gulf. *Journal of Geophysical Research*, 108(C12), 3991,
778 <https://doi.org/10.1029/2003JC001881>.
- 779 Kämpf, J., and M. Sadrienasab, 2006: The circulation of the Persian Gulf: a numerical study. *Ocean*
780 *Science*, 2, 27–41, <https://doi.org/10.5194/os-2-27-2006>.
- 781 Kopp, R. E., R. M. Horton, C. M. Little, J. X. Mitrovica, M. Oppenheimer, D. J. Ras-
782 mussen, B. H. Strauss, and C. Tebaldi, 2014: Probabilistic 21st and 22nd century sea-

783 level projections at a global network of tide-gauge sites. *Earth's Future*, 2, 383–406,
784 <https://doi.org/10.1002/2014EF000239>.

785 Kopp, R. E., R. M. DeConto, D. A. Bader, C. C. Hay, R. M. Horton, S. Kulp, M. Oppen-
786 heimer, D. Pollard, and B. H. Strauss, 2017: Evolving Understanding of Antarctic Ice-Sheet
787 Physics and Ambiguity in Probabilistic Sea-Level Projections. *Earth's Future*, 5, 1217–1233,
788 <https://doi.org/10.1002/2017EF000663>.

789 Lafta, A. A., S. A. Altaei, and N. H. Al-Hashimi, 2020: Impacts of potential sea-level rise on tidal
790 dynamics in Khor Abdullah and Khor Al-Zubair, northwest of Arabian Gulf. *Earth Systems and*
791 *Environment*, 4, 93–105, <https://doi.org/10.1007/s41748-020-00147-9>.

792 Landerer, F. W., and D. L. Volkov, 2013: The anatomy of recent large sea level
793 fluctuations in the Mediterranean Sea. *Geophysical Research Letters*, 40, 553–557,
794 <https://doi.org/10.1002/grl.50140>.

795 Landerer, F. W., F. M. Flechtner, H. Save, F. H. Webb, T. Bandikova, W. I. Bertiger, S. V.
796 Bettadpur, S. H. Byun, C. Dahle, H. Dobslaw, E. Fahnestock, N. Harvey, Z. Kang, G. L. H.
797 Kruizinga, B. D. Loomis, C. McCullough, M. Murböck, P. Nagel, M. Paik, N. Pie, S. Poole,
798 D. Strelakov, M. E. Tamisiea, F. Wang, M. M. Watkins, H.-Y. Wen, D. N. Wiese, and D.-N.
799 Yuan, 2020: Extending the Global Mass Change Data Record: GRACE Follow-On Instru-
800 ment and Science Data Performance. *Geophysical Research Letters*, 47(12), e2020GL088306,
801 <https://doi.org/10.1029/2020GL088306>.

802 Large, W. G., and S. G. Yeager, 2004: Diurnal to Decadal Global Forcing For Ocean and Sea-Ice
803 Models: The Data Sets and Flux Climatologies. NCAR/TN-460+ STR, NCAR Technical Note,
804 112 pp.

805 Larson, A., 2007: Oil. The Geopolitics of Oil and Natural Gas. *New England Journal of Public*
806 *Policy*, 21(2), 215–219, <https://scholarworks.umb.edu/nejpp/vol21/iss2/18>.

807 Legeais, J.-F., M. Ablain, L. Zawadzki, H. Zuo, J. A. Johannessen, M. G. Scharffenberg, L.
808 Fenoglio-Marc, M. J. Fernandes, O. B. Andersen, S. Rudenko, P. Cipollini, G. D. Quartly, M.
809 Passaro, A. Cazenave, and J. Benveniste, 2017.: An improved and homogeneous altimeter sea
810 level record from the ESA Climate Change Initiative. *Earth System Science Data*, 10, 281–301,
811 <https://doi.org/10.5194/essd-10-281-2018>.

812 Long, X., M. J. Widlansky, F. Schloesser, P. R. Thompson, H. Annamalai, M. A. Merrifield, and
813 H. Yoon, 2020: Higher Sea Levels at Hawaii Caused by Strong El Niño and Weak Trade Winds.
814 *Journal of Climate*, 33, 3037–3059, <https://doi.org/10.1175/JCLI-D-19-0221.1>.

815 Loomis, B. D., and S. B. Luthcke, 2017: Mass evolution of Mediterranean, Black, Red, and Caspian
816 Seas from GRACE and altimetry: accuracy assessment and solution calibration. *Journal of*
817 *Geodesy*, 91, 195–206, <https://doi.org/10.1007/s00190-016-0952-3>.

818 Mathers, E. L., and P. L. Woodworth, 2001: Departures from the local inverse barometer model
819 observed in altimeter and tide gauge data and in a global barotropic numerical model. *Journal*
820 *of Geophysical Research*, 106(C4), 9657–6972, <https://doi.org/10.1029/2000JC000241>.

821 Mathers, E. L., and P. L. Woodworth, 2004: A study of departures from the inverse-barometer
822 response of sea level to air-pressure forcing at a period of 5 days. *Quarterly Journal of the Royal*
823 *Meteorological Society*, 130, 725–738, <https://doi.org/10.1256/qj.03.46>.

824 Meyssignac, B., C. G. Piecuch, C. J. Merchant, M.-F. Racault, H. Palanisamy, C. MacIntosh, S.
825 Sathyendranath, and R. Brewin, 2017: Causes of the Regional Variability in Observed Sea Level,

826 Sea Surface Temperature and Ocean Colour Over the Period 1993–2011. *Surveys in Geophysics*,
827 38, 187–215, <https://doi.org/10.1007/s10712-016-9383-1>.

828 Nerem, R. S., B. D. Beckley, J. T. Fasullo, B. D. Hamlington, D. Masters, and G. T. Mitchum, 2018:
829 Climate-change-driven accelerated sea-level rise detected in the altimeter era. *Proceedings of the*
830 *National Academy of Sciences*, 115(9), 2022–2025, <https://doi.org/10.1073/pnas.1717312115> .

831 Oliver, E. C. J., and K. R. Thompson, 2010: Madden-Julian Oscillation and sea
832 level: local and remote forcing. *Journal of Geophysical Research*, 115(C01003),
833 <https://doi.org/10.1029/2009JC005337>.

834 Osman, M. M., 1984: Variation of sea level at Port-Sudan. *International Hydrographic Review*,
835 61(2).

836 Patzert, W. C., 1974: Wind-induced reversal in Red Sea circulation. *Deep-Sea Research*, 21(2),
837 109–121, [https://doi.org/10.1016/0011-7471\(74\)90068-0](https://doi.org/10.1016/0011-7471(74)90068-0).

838 Permanent Service for Mean Sea Level (PSMSL), 2020: “Tide Gauge Data”, Retrieved 1 Jul 2019
839 from <http://www.psmsl.org/data/obtaining/>.

840 Piecuch, C. G., and R. M. Ponte, 2015: A wind-driven nonseasonal barotropic fluctuation of the
841 Canadian inland seas. *Ocean Science*, 11, 175–185, <https://doi.org/10.5194/os-11-175-2015>.

842 Piecuch, C. G., K. Bittermann, A. C. Kemp, R. M. Ponte, C. M. Little, S. E. Engelhart,
843 and S. J. Lentz, 2018: River-discharge effects on United States Atlantic and Gulf coast
844 sea-level changes. *Proceedings of the National Academy of Sciences*, 115(30), 7729–7734,
845 <https://doi.org/10.1073/pnas.1805428115>.

846 Piecuch, C. G., Landerer, F. W., and R. M. Ponte, 2018b: Tide gauge records reveal
847 improved processing of Gravity Recovery and Climate Experiment time-variable mass

848 solutions over the coastal ocean. *Geophysical Journal International*, 214, 1401–1412,
849 <https://doi.org/10.1093/gji/ggy207>.

850 Piecuch, C. G., F. M. Calafat, S. Dangendorf, and G. Jordà, 2019: The Ability of Barotropic
851 Models to Simulate Historical Mean Sea Level Changes from Coastal Tide Gauge Data. *Surveys
852 in Geophysics*, 40, 1399–1435, <https://doi.org/10.1007/s10712-019-09537-9>.

853 Ponte, R. M., 1992: The Sea Level Response of a Stratified Ocean to Barometric Pres-
854 sure Forcing. *Journal of Physical Oceanography*, 22, 109–113, [https://doi.org/10.1175/1520-0485\(1992\)022<0109:TSLROA>2.0.CO;2](https://doi.org/10.1175/1520-0485(1992)022<0109:TSLROA>2.0.CO;2).

856 Ponte, R. M., 1994: Understanding the relation between wind- and pressure-
857 driven sea level variability. *Journal of Geophysical Research*, 99(C4), 8033–8039,
858 <https://doi.org/10.1029/94JC00217>.

859 Ponte, R. M., 2006: Oceanic Response to Surface Loading Effects Neglected
860 in Volume-Conserving Models. *Journal of Physical Oceanography*, 36, 426–434,
861 <https://doi.org/10.1175/JPO2843.1>.

862 Privett, D. W., 1959: Monthly charts of evaporation from the N. Indian Ocean (including the Red
863 Sea and the Persian Gulf). *Quarterly Journal of the Royal Meteorological Society*, 85, 424–428,
864 <https://doi.org/10.1002/qj.49708536614>.

865 Quartly, G. D., J.-F. Legeais, M. Ablain, L. Zawadzki, M. J. Fernandes, S. Rudenko, L. Carrère,
866 P. N. García, P. Cipollini, O. B. Andersen, J.-C. Poisson, S. Mbajon Njiche, A. Cazenave, and
867 J. Benveniste, 2017: A new phase in the production of quality-controlled sea level data. *Earth
868 System Science Data*, 9, 557–572, <https://doi.org/10.5194/essd-9-557-2017>.

- 869 Ray, R. D., and G. Foster, 2016: Future nuisance flooding at Boston caused by astronomical tides
870 alone. *Earth's Future*, 4, 578–587, <https://doi.org/10.1002/2016EF000423>.
- 871 Reynolds, R. M., 1993: Physical oceanography of the Gulf, Strait of Hormuz, and the Gulf
872 of Oman—results from the *Mt Mitchell* Expedition. *Marine Pollution Bulletin*, 27, 35–59,
873 [https://doi.org/10.1016/0025-326X\(93\)90007-7](https://doi.org/10.1016/0025-326X(93)90007-7).
- 874 Rohith, B., A. Paul, F. Durand, L. Testut, S. Prerna, M. Afroosa, S. S. V. S. Ramkrishna, and
875 S. S. C. Shenoi, 2019: Basin-wide sea level coherency in the tropical Indian Ocean driven by
876 Madden-Julian Oscillation. *Nature Communications*, 10, 1257, [https://doi.org/10.1038/s41467-](https://doi.org/10.1038/s41467-019-09243-5)
877 019-09243-5.
- 878 Sharaf El Din, S. H., 1990: Sea level variation along the western coast of the Arabian Gulf.
879 *International Hydrographic Review*, 67(1), 103–109.
- 880 Siddig, N. A., A. M. Al-Subhi, and M. A. Alsaafani, 2019: Tide and mean sea level trend in the west
881 coast of the Arabian Gulf from tide gauges and multi-missions satellite altimeter. *Oceanologia*,
882 61, 401–411, <https://doi.org/10.1016/j.oceano.2019.05.003>.
- 883 Sofianos, S. S., and Johns, W. E., 2001: Wind induced sea level variability in the Red Sea.
884 *Geophysical Research Letters*, 28(16), 3175–3178, <https://doi.org/10.1029/2000GL012442>.
- 885 Sultan, S. A. R., F. Ahmad, N. M. Elghribi, and A. M. Al-Subhi, 1995a: An analy-
886 sis of Arabian Gulf mean sea level. *Continental Shelf Research*, 15(11/12), 1471–1482,
887 [https://doi.org/10.1016/0278-4343\(94\)00081-W](https://doi.org/10.1016/0278-4343(94)00081-W).
- 888 Sultan, S. A. R., Ahmad, F., and Elghribi, N. M., 1995b: Sea level variability in the central Red
889 Sea. *Oceanologica Acta*, 18(6).

- 890 Sultan, S. A. R., Ahmad, F., and El-Hassan, A., 1995c: Seasonal variations of the sea
891 level in the central part of the Red Sea. *Estuarine, Coastal and Shelf Science*, 40, 1–8,
892 [https://doi.org/10.1016/0272-7714\(95\)90008-X](https://doi.org/10.1016/0272-7714(95)90008-X).
- 893 Sultan, S. A. R., Ahmad, F., and Nassar, D., 1996: Relative contribution of external sources of
894 mean sea-level variations at Port Sudan, Red Sea. *Estuarine, Coastal and Shelf Science*, 42,
895 19–30, <https://doi.org/10.1006/ecss.1996.0002>.
- 896 Sultan, S. A. R., M. O. Moamar, N. M. El-Ghribi, and R. Williams, 2000: Sea level changes along
897 the Saudi coast of the Arabian Gulf. *Indian Journal of Marine Sciences*, 29, 191–200.
- 898 Sultan, S. A. R., and Elghribi, N. M., 2003: Sea level changes in the central part of the Red Sea.
899 *Indian Journal of Marine Sciences*, 32(2), 114–122.
- 900 Suresh, I., J. Vialard, M. Lengaigne, W. Han, J. McCreary, F. Durand, and P. M.
901 Muraleedharan, 2013: Origins of wind-driven intraseasonal sea level variations in the
902 North Indian Ocean coastal waveguide. *Geophysical Research Letters*, 40, 5740–5744,
903 <https://doi.org/10.1002/2013GL058312>.
- 904 Suresh, I., Vialard, J., Izumo, T., Lengaigne, M., Han, W., McCreary, J., and Muraleedha-
905 ran, P. M., 2016: Dominant role of winds near Sri Lanka in driving seasonal sea level
906 variations along the west coast of India. *Geophysical Research Letters*, 43, 7028–7035,
907 <https://doi.org/10.1002/2016GL069976>
- 908 Sweet, W. V., M. Menendez, A. Genz, J. Obeysekera, J. Park, and J. J. Marra, 2017: In Tide’s Way:
909 Southeast Florida’s September 2015 Sunny-day Flood. *Bulletin of the American Meteorological*
910 *Society*, 97(12), S25–S30, <https://doi.org/10.1175/BAMS-D-16-0117.1>.

911 Swift, S. A., and A. S. Bower, 2003: Formation and circulation of dense water in the Persian/Arabian
912 Gulf. *Journal of Geophysical Research*, 108(C1), 3004, <https://doi.org/10.1029/2002JC001360>.

913 Thoppil, P. G., and P. J. Hogan, 2010: A Modeling Study of Circulation and
914 Eddies in the Persian Gulf. *Journal of Physical Oceanography*, 40, 2122–2134,
915 <https://doi.org/10.1175/2010JPO4227.1>.

916 Tregoning, P., K. Lambeck, and G. Ramillien, 2008: GRACE estimates of sea surface height
917 anomalies in the Gulf of Carpentaria, Australia. *Earth and Planetary Science Letters*, 271,
918 241–244, <https://doi.org/10.1016/j.epsl.2008.04.018>.

919 Tsujino, H., S. Urakawa, H. Nakano, R. J. Small, W. M. Kim, S. G. Yeager, G. Danabasoglu, T.
920 Suzuki, J. L. Bamber, M. Bentsen, C. W. Böning, A. Bozec, E. P. Chassignet, E. Curchitser, F. B.
921 Dias, P. J. Durack, S. M. Griffies, Y. Harada, M. Ilicak, S. A. Josey, C. Kobayashi, S. Kobayashi, Y.
922 Komuro, W. G. Large, J. Le Sommer, S. J. Marsland, S. Masina, M. Scheinert, H. Tomita, M. Val-
923 divieso, and D. Yamazaki, 2018: JRA-55 based surface dataset for driving ocean?sea-ice models
924 (JRA55-do). *Ocean Modelling*, 130, 79–139, <https://doi.org/10.1016/j.ocemod.2018.07.002>.

925 Vinogradova, N. T., R. M. Ponte, and D. Stammer, 2007: Relation between sea level and bottom
926 pressure and the vertical dependence of oceanic variability. *Geophysical Research Letters*, 34,
927 L03608, <https://doi.org/10.1029/2006GL028588>.

928 Vivier, F., K. A. Kelly, and L. Thompson, 1999: Contributions of wind forcing, waves, and surface
929 heating to sea surface height observations in the Pacific Ocean. *Journal of Geophysical Research*,
930 104(C9), 20767–20788, <https://doi.org/10.1029/1999JC900096>.

931 Volkov, D. L., W. E. Johns, and T. B. Belonenko, 2016: Dynamic response of the Black Sea
932 elevation to intraseasonal fluctuations of the Mediterranean sea level. *Geophysical Research*

- 933 *Letters*, 43, 283–290, <https://doi.org/10.1002/2015GL066876>.
- 934 von Storch, H., and F. W. Zwiers, 1999: *Statistical Analysis in Climate Research*, Cambridge
935 University Press, 496 pp.
- 936 Wahr, J. W., D. A. Smeed, E. Leuliette, and S. Swenson, 2014: Seasonal variability of the Red
937 Sea, from satellite gravimetry, radar altimetry, and in situ observations. *Journal of Geophysical
938 Research Oceans*, 119, 5091–5104, <https://doi.org/10.1002/2014JC010161>.
- 939 Waliser, D. E., R. Murtugudde, and L. E. Lucas, 2003: Indo-Pacific Ocean response to atmospheric
940 intraseasonal variability: 1. Austral summer and the Madden-Julian Oscillation. *Journal of
941 Geophysical Research*, 108(C5), 3160, <https://doi.org/10.1029/2002JC001620>.
- 942 Waliser, D. E., R. Murtugudde, and L. E. Lucas, 2003: Indo-Pacific Ocean response to atmo-
943 spheric intraseasonal variability: 2. Boreal summer and the Intraseasonal Oscillation. *Journal
944 of Geophysical Research*, 109(C03030), 3160, <https://doi.org/10.1029/2003JC002002>.
- 945 Wang, J., J. Wang, and X. Cheng, 2015: Mass-induced sea level variations in the Gulf of Carpen-
946 taria. *Journal of Oceanography*, 71, 449–461, <https://doi.org/10.1007/s10872-015-0304-6>.
- 947 Watkins, M. M., D. N. Wiese, D.-H. Yuan, C. Boening, and F. W. Landerer, 2015: Im-
948 proved methods for observing Earth's time variable mass distribution with GRACE using
949 spherical cap mascons. *Journal of Geophysical Research: Solid Earth*, 120, 2648–2671,
950 <https://doi.org/10.1002/2014JB011547>.
- 951 Wiese, D. N., F. W. Landerer, and M. M. Watkins, 2016: Quantifying and reducing leakage errors
952 in the JPL RL05M GRACE mascon solution. *Water Resources Research*, 52(9), 7490–7502,
953 <https://doi.org/10.1002/2016WR019344>.

- 954 Wouters, B., and D. Chambers, 2010: Analysis of seasonal ocean bottom pressure vari-
955 ability in the Gulf of Thailand from GRACE. *Global and Planetary Change*, 74, 76–81,
956 <https://doi.org/10.1016/j.gloplacha.2010.08.002>.
- 957 Wunsch, C., and D. Stammer, 1997: Atmospheric loading and the “inverted barometer” effect.
958 *Reviews in Geophysics*, 35(1), 79–107, <https://doi.org/10.1029/96RG03037>.
- 959 Yao, F., and W. E. Johns, 2010: A HYCOM modeling study of the Persian Gulf: 1.
960 Model configurations and surface circulation. *Journal of Geophysical Research*, 115(C11017),
961 <https://doi.org/10.1029/2009JC005781>.
- 962 Yu, L., and R. A. Weller, 2007: Objectively Analyzed Air-Sea Heat Fluxes for the Global Ice-
963 Free Oceans (1981–2005). *Bulletin of the American Meteorological Society*, 88(4), 527–540,
964 <https://doi.org/10.1175/BAMS-88-4-527>.

965 **LIST OF TABLES**

966 **Table 1.** Data sources. All websites are current as of this writing. 48

967 **Table 2.** Description of tide-gauge records. Asterisk indicates metric data without com-
 968 plete datum histories. 49

969 **Table 3.** Descriptions of and, where applicable, reasonable values for variables and
 970 parameters in governing equations. [†]Values of the friction coefficient r are
 971 uncertain. Previous studies variously use values ranging from as small as
 972 $4 \times 10^{-5} \text{ m s}^{-1}$ (e.g., Ponte, 1994) to as large as $2 \times 10^{-2} \text{ m s}^{-1}$ (e.g., Ponte,
 973 2006). Values in the table represent a reasonable, physically plausible range
 974 based on choices made in previous studies. 50

975 **Table 4.** Estimates of the scaling coefficients (z_j) and phase angles (θ_j) in Eq. (4). The
 976 theoretical ranges are determined by averaging Eqs. (5)–(12) over the range
 977 $\omega = 2\pi / (6 \text{ months})$ to $2\pi / (2 \text{ months})$ using the constant values for σ , L , ρ ,
 978 g , and H and the minimum and maximum values for λ tabulated in Table 3.
 979 Empirical values are determined through multiple linear regression involving $\bar{\zeta}$
 980 and $\bar{\zeta}_0$ from altimetry, τ and \bar{p} from ERA-Interim, and \bar{q} based on JRA55-do,
 981 GPCP, and OAFflux, and are presented as 95% confidence intervals estimated
 982 based on bootstrapping. Scaling coefficients are given to one decimal point and
 983 phase angles are rounded to the nearest degree. 51

Data set	Location
Altimetry	ftp://anon-ftp.ceda.ac.uk/neodc/esacci/sea_level/data/L4/MSLA/v2.0/
GRACE	https://podaac.jpl.nasa.gov/dataset/TELLUS_GRAC-GRFO_MASCON_CRI_GRID_RL06_V2
Tide gauges	https://www.psmsl.org/data/obtaining/complete.php
ERA-Interim	http://cmip5.who.edu/?page_id=566
GPCP	https://psl.noaa.gov/data/gridded/data.gpcp.html
OAFlux	ftp://ftp.who.edu/pub/science/oaflux/data_v3/monthly/evaporation/
JRA55-do	http://amaterasu.ees.hokudai.ac.jp/~tsujino/JRA55-do-suppl/runoff/

TABLE 1. Data sources. All websites are current as of this writing.

Station Name	Nation	PSMSL Identifier	Longitude (°E)	Latitude (°N)	Span	Completeness
Mina Sulman	Bahrain	1494	50.6	26.2	1979–2006	66.1%
Emam Hassan*	Iran	1868	50.3	29.8	1995–2006	91.7%
Bushehr*	Iran	1939	50.8	28.9	2004–2006	100.0%
Kangan*	Iran	1869	52.1	27.8	1995–2006	98.6%
Shahid Rajaei*	Iran	1870	56.1	27.1	1995–2006	100.0%

TABLE 2. Description of tide-gauge records. Asterisk indicates metric data without complete datum histories.

Parameter	Description	Value
ζ	Ocean Dynamic Sea Level	—
τ	Mean Wind Stress Along Strait of Hormuz	—
q	Surface Freshwater Flux	—
p	Barometric Pressure	—
ζ_0	Ocean Dynamic Sea Level in Gulf of Oman	—
$\bar{\cdot}$	Spatial Average over Persian Gulf	—
S	Surface Area of Persian Gulf	$2.2 \times 10^5 \text{ km}^2$
H	Average Depth of Persian Gulf	30 m
L	Length of Strait of Hormuz	400 km
W	Width of Strait of Hormuz	100 km
g	Gravitational Acceleration	9.81 m s^{-2}
ρ	Ocean Density	1029 kg m^{-3}
r	Friction Coefficient [†]	$1 \times 10^{-3} - 1 \times 10^{-2} \text{ m s}^{-1}$
σ	Inverse Resonance Timescale	$1.8 \times 10^{-5} \text{ s}^{-1}$
λ	Inverse Frictional Timescale	$3.3 \times 10^{-5} - 3.3 \times 10^{-4} \text{ s}^{-1}$

984 TABLE 3. Descriptions of and, where applicable, reasonable values for variables and parameters in governing
985 equations. [†]Values of the friction coefficient r are uncertain. Previous studies variously use values ranging from
986 as small as $4 \times 10^{-5} \text{ m s}^{-1}$ (e.g., Ponte, 1994) to as large as $2 \times 10^{-2} \text{ m s}^{-1}$ (e.g., Ponte, 2006). Values in the table
987 represent a reasonable, physically plausible range based on choices made in previous studies.

Parameter (Units)	Theoretical Range	Empirical Value
z_{ζ_0} (unitless)	0.8–1.0	1.0 ± 0.2
θ_{ζ_0} (degrees)	5–38	5 ± 10
z_{τ} (m Pa ⁻¹)	1.0–1.3	1.5 ± 0.5
θ_{τ} (degrees)	5–38	30 ± 25
$z_{\bar{q}}$ (days)	1.2–9.0	9.4 ± 3.7
$\theta_{\bar{q}}$ (degrees)	3–38	30 ± 27
$z_{\bar{p}}$ (cm mb ⁻¹)	0.1–0.5	0.8 ± 0.5
$\theta_{\bar{p}}$ (degrees)	56–87	65 ± 52

988 TABLE 4. Estimates of the scaling coefficients (z_j) and phase angles (θ_j) in Eq. (4). The theoretical ranges are
989 determined by averaging Eqs. (5)–(12) over the range $\omega = 2\pi / (6 \text{ months})$ to $2\pi / (2 \text{ months})$ using the constant
990 values for σ , L , ρ , g , and H and the minimum and maximum values for λ tabulated in Table 3. Empirical values
991 are determined through multiple linear regression involving $\bar{\zeta}$ and ζ_0 from altimetry, τ and \bar{p} from ERA-Interim,
992 and \bar{q} based on JRA55-do, GPCP, and OAFflux, and are presented as 95% confidence intervals estimated based
993 on bootstrapping. Scaling coefficients are given to one decimal point and phase angles are rounded to the nearest
994 degree.

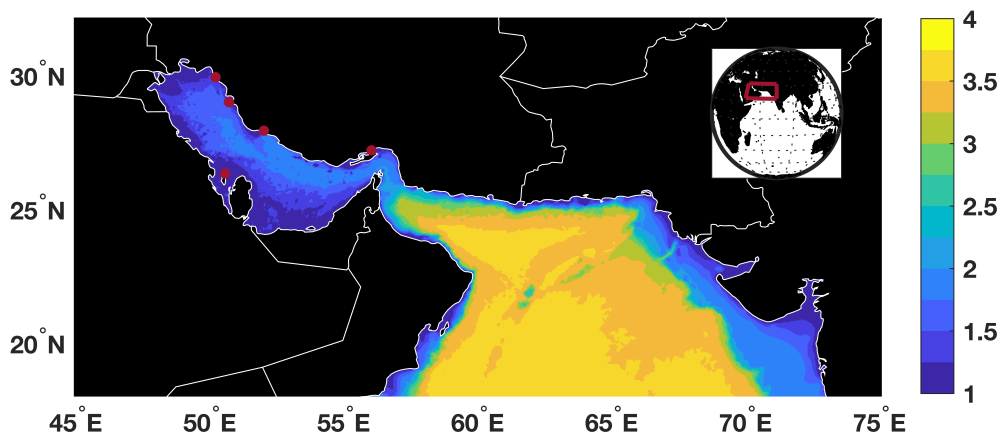
LIST OF FIGURES

995		
996	Fig. 1.	Study area. White lines indicate national boundaries. Color shading identifies ocean depth. (Note the logarithmic scale bar and units of \log_{10} m.) Red dots denote locations of tide gauges (Table 2). Inset shows the study area in a global context.
997		54
998		
999	Fig. 2.	Monthly ocean dynamic sea level in the Persian Gulf between November 2002 and March 2015 from satellite altimetry (gray, black, blue) and tide gauges (oranges). The satellite-altimetry data are spatially averaged over the Persian Gulf whereas the tide-gauge data represent a composite average over five sites (Figure 1). The raw monthly altimetry data are shown in gray, whereas the black and blue indicate the altimetry data with filtering applied to isolate nonseasonal and intraseasonal timescales, respectively. The tide-gauge data (orange) have been filtered to isolate intraseasonal periods and adjusted for the inverted-barometer effect. The standard deviations of the gray, black, blue, and orange time series are 4.7, 3.5, 3.0, and 2.5 cm, respectively.
1000		55
1001		
1002		
1003		
1004		
1005		
1006		
1007		
1008	Fig. 3.	(a.) Spatial pattern (eigenvector) of the first ζ EOF mode across the Persian Gulf from intraseasonal altimetry data. Units are cm. (b.) Local ζ variance explained by the first EOF mode. Units are percent of total variance.
1009		56
1010		
1011	Fig. 4.	Principal-component time series of the first EOF modes from altimetry ζ (black) and GRACE R_m (blue) over the Persian Gulf. Time series have been normalized to unit variance (physical units are shown for the eigenvectors in Figures 3 and 5).
1012		57
1013		
1014	Fig. 5.	(a.) Spatial pattern (eigenvector) of the first R_m EOF mode across the Persian Gulf from intraseasonal GRACE data. Units are cm. (b.) Local R_m variance explained by the first EOF mode. Units are percent of total variance.
1015		58
1016		
1017	Fig. 6.	(a.) Time series of intraseasonal $\bar{\zeta}$ from satellite altimetry (black) and the results of the multiple linear regression model (blue). Units are cm. (b.) Breakdown of contributors to regression model—boundary forcing ζ_0 (orange), wind stress τ (green), freshwater flux \bar{q} (blue), and barometric pressure \bar{p} (red). Units are cm.
1018		59
1019		
1020		
1021	Fig. 7.	Amplitude of $\bar{\zeta}$ response to boundary forcing ζ_0 (orange), wind stress τ (green), freshwater flux \bar{q} (blue), and barometric pressure \bar{p} (red) as a function of period. Values are based on Eqs. (6), (8), (10), (12) using parameter values from Table 3. Upper and lower lines are bounds determined by the range of friction coefficient r . See text for more details. Gray shading indicates intraseasonal periods of primary interest here.
1022		60
1023		
1024		
1025		
1026	Fig. 8.	Shading represents correlation coefficients between Gulf of Oman ζ_0 and ζ from altimetry over the Equatorial and North Indian Ocean. Dots are the same, but based on ζ from available tide gauges. Light shading indicates values that are not distinguishable from zero at the 95% confidence level (assuming 100 degrees of freedom).
1027		61
1028		
1029		
1030	Fig. 9.	Shading represents correlation coefficients between Gulf of Oman ζ_0 and $\mathcal{H}(\zeta)$ from altimetry over the Equatorial and North Indian Ocean. Light shading indicates values that are not distinguishable from zero at the 95% confidence level (assuming 100 degrees of freedom).
1031		62
1032		
1033	Fig. 10.	Correlation coefficient between Gulf of Oman ζ_0 and either (a.) R_m from GRACE or (b.) $\mathcal{H}(R_m)$ over the Indian Ocean. Light shading indicates values that are not distinguishable from zero at the 95% confidence level (assuming 100 degrees of freedom).
1034		63
1035		

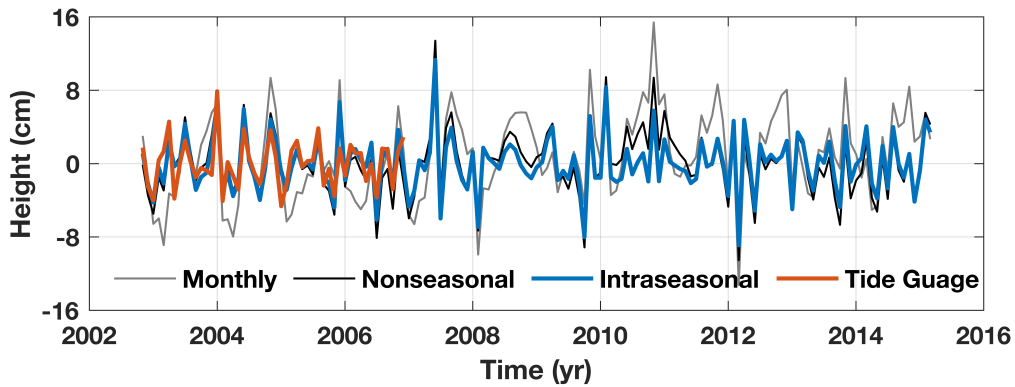
1036 **Fig. 11.** Shading represents correlation coefficients between Gulf of Oman ζ_0 and altimetric ζ else-
 1037 where over the Equatorial and North Indian Ocean 1 month earlier (i.e., ζ_0 is lagging ζ
 1038 elsewhere). Dots are the same, but based on ζ from available tide gauges. Light shading
 1039 indicates values that are not distinguishable from zero at the 95% confidence level (assuming
 1040 100 degrees of freedom). 64

1041 **Fig. 12.** Shading represents correlation coefficients between Gulf of Oman ζ_0 and altimetric ζ else-
 1042 where over the Equatorial and North Indian Ocean 2 months earlier (i.e., ζ_0 is lagging ζ
 1043 elsewhere). Dots are the same, but based on ζ from available tide gauges. Light shading
 1044 indicates values that are not distinguishable from zero at the 95% confidence level (assuming
 1045 100 degrees of freedom). 65

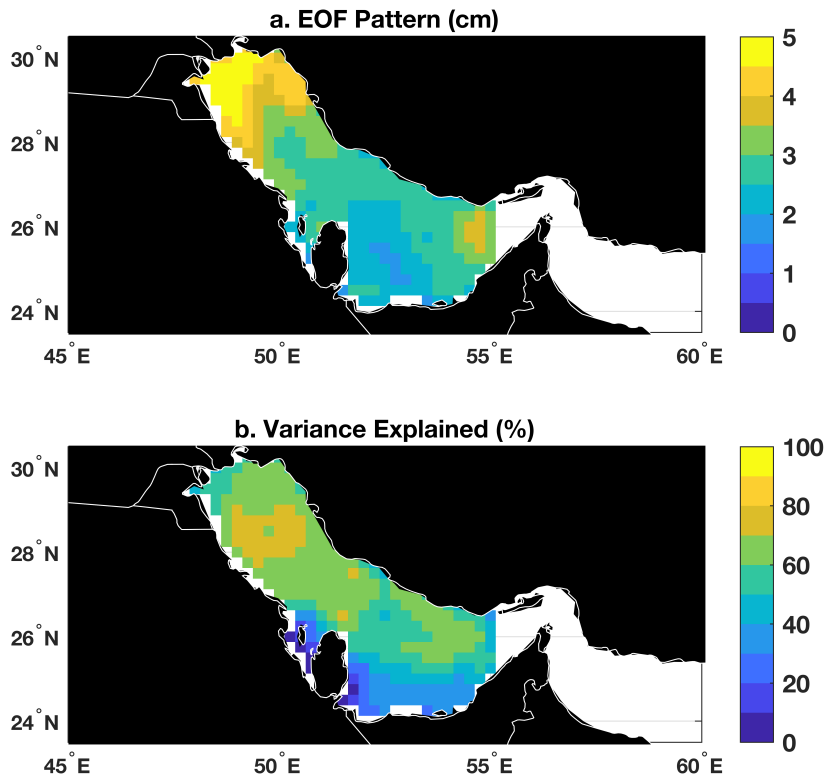
1046 **Fig. A1.** Amplitude of vWH response to boundary forcing ζ_0 (orange), wind stress τ (green), fresh-
 1047 water flux \bar{q} (blue), and barometric pressure \bar{p} (red) as a function of period. Values are based
 1048 on Eqs. (A4), (A6), (A8), (A10) using parameter values from Table 3. Upper and lower
 1049 lines are bounds determined by the range of friction coefficient r . See text for more details.
 1050 Gray shading indicates intraseasonal periods of primary interest here. Dashed black line is
 1051 the standard deviation of estimated transport described in the Discussion section. 66



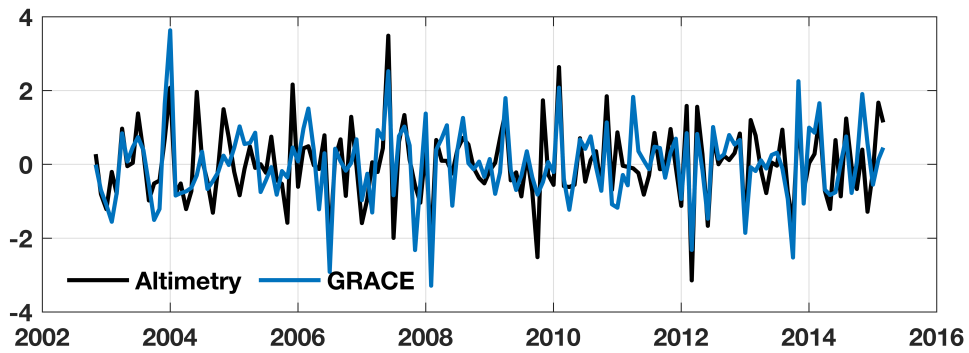
1052 FIG. 1. Study area. White lines indicate national boundaries. Color shading identifies ocean depth. (Note the
 1053 logarithmic scale bar and units of \log_{10} m.) Red dots denote locations of tide gauges (Table 2). Inset shows the
 1054 study area in a global context.



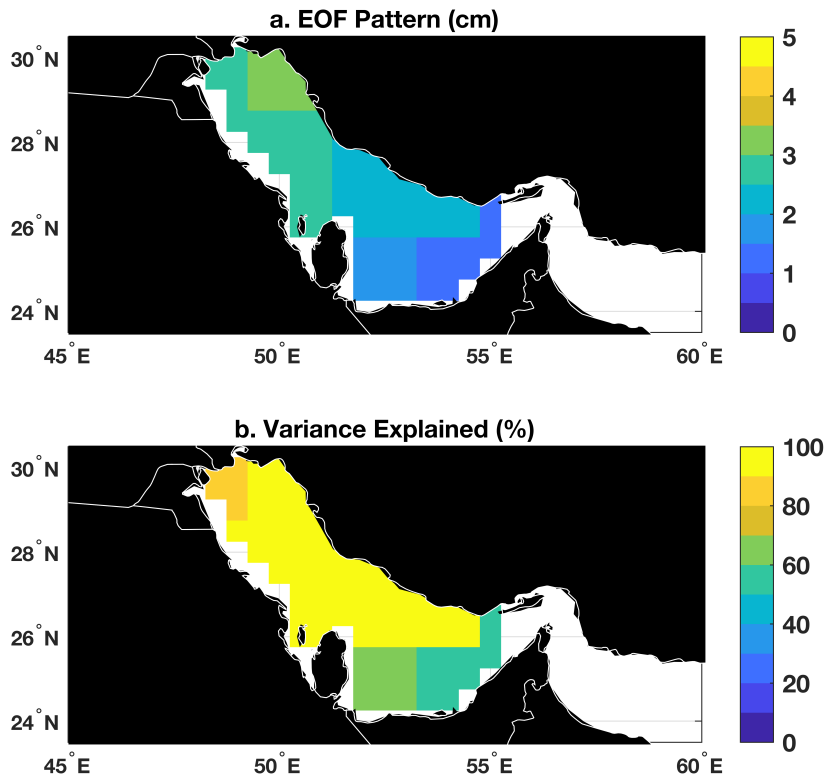
1055 FIG. 2. Monthly ocean dynamic sea level in the Persian Gulf between November 2002 and March 2015 from
 1056 satellite altimetry (gray, black, blue) and tide gauges (oranges). The satellite-altimetry data are spatially averaged
 1057 over the Persian Gulf whereas the tide-gauge data represent a composite average over five sites (Figure 1). The
 1058 raw monthly altimetry data are shown in gray, whereas the black and blue indicate the altimetry data with filtering
 1059 applied to isolate nonseasonal and intraseasonal timescales, respectively. The tide-gauge data (orange) have been
 1060 filtered to isolate intraseasonal periods and adjusted for the inverted-barometer effect. The standard deviations
 1061 of the gray, black, blue, and orange time series are 4.7, 3.5, 3.0, and 2.5 cm, respectively.



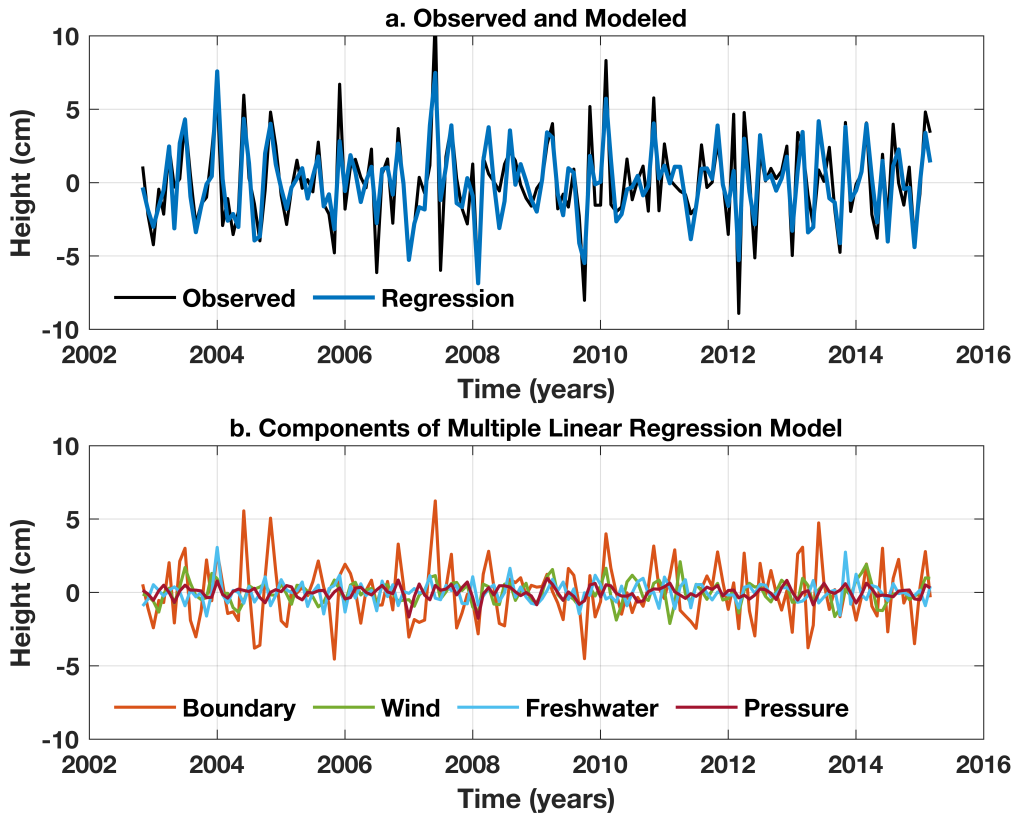
1062 FIG. 3. (a.) Spatial pattern (eigenvector) of the first ζ EOF mode across the Persian Gulf from intraseasonal
 1063 altimetry data. Units are cm. (b.) Local ζ variance explained by the first EOF mode. Units are percent of total
 1064 variance.



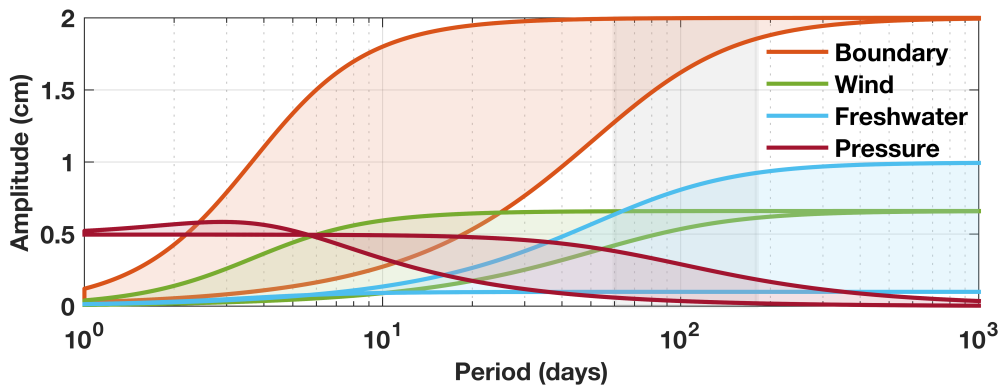
1065 FIG. 4. Principal-component time series of the first EOF modes from altimetry ζ (black) and GRACE R_m
 1066 (blue) over the Persian Gulf. Time series have been normalized to unit variance (physical units are shown for the
 1067 eigenvectors in Figures 3 and 5).



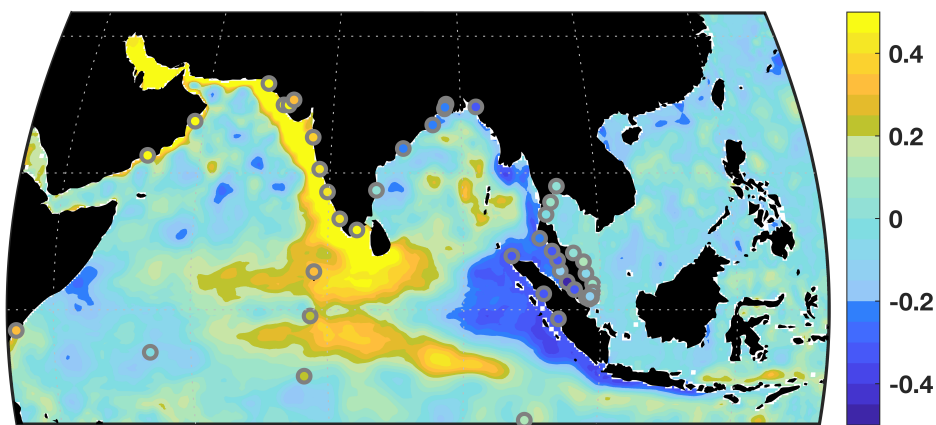
1068 FIG. 5. **(a.)** Spatial pattern (eigenvector) of the first R_m EOF mode across the Persian Gulf from intraseasonal
 1069 GRACE data. Units are cm. **(b.)** Local R_m variance explained by the first EOF mode. Units are percent of total
 1070 variance.



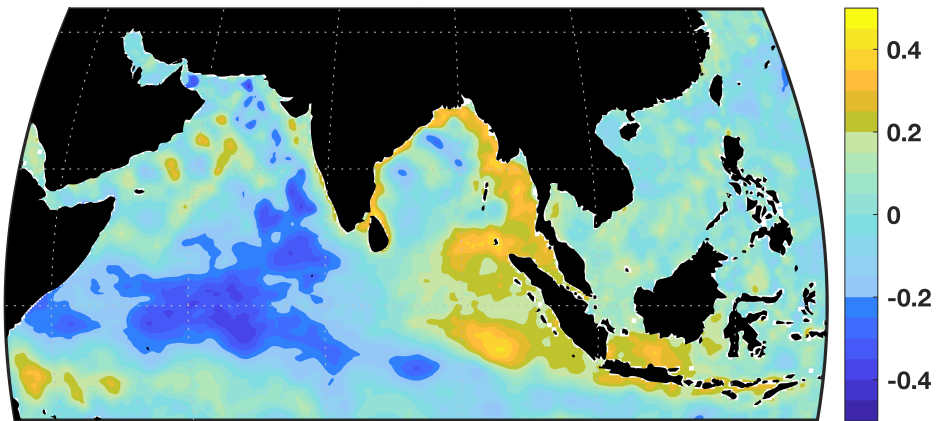
1071 FIG. 6. (a.) Time series of intraseasonal $\bar{\zeta}$ from satellite altimetry (black) and the results of the multiple linear
 1072 regression model (blue). Units are cm. (b.) Breakdown of contributors to regression model—boundary forcing
 1073 ζ_0 (orange), wind stress τ (green), freshwater flux \bar{q} (blue), and barometric pressure \bar{p} (red). Units are cm.



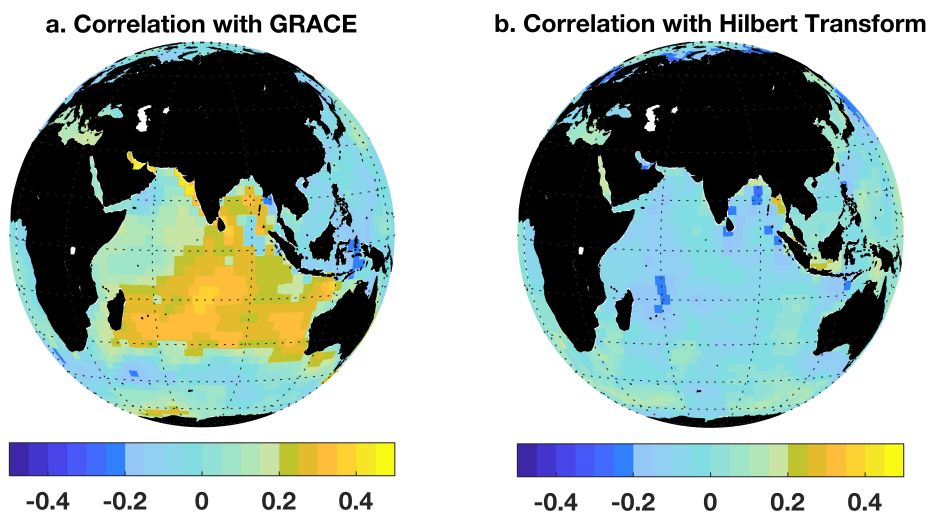
1074 FIG. 7. Amplitude of $\bar{\zeta}$ response to boundary forcing ζ_0 (orange), wind stress τ (green), freshwater flux \bar{q}
 1075 (blue), and barometric pressure \bar{p} (red) as a function of period. Values are based on Eqs. (6), (8), (10), (12) using
 1076 parameter values from Table 3. Upper and lower lines are bounds determined by the range of friction coefficient
 1077 r . See text for more details. Gray shading indicates intraseasonal periods of primary interest here.



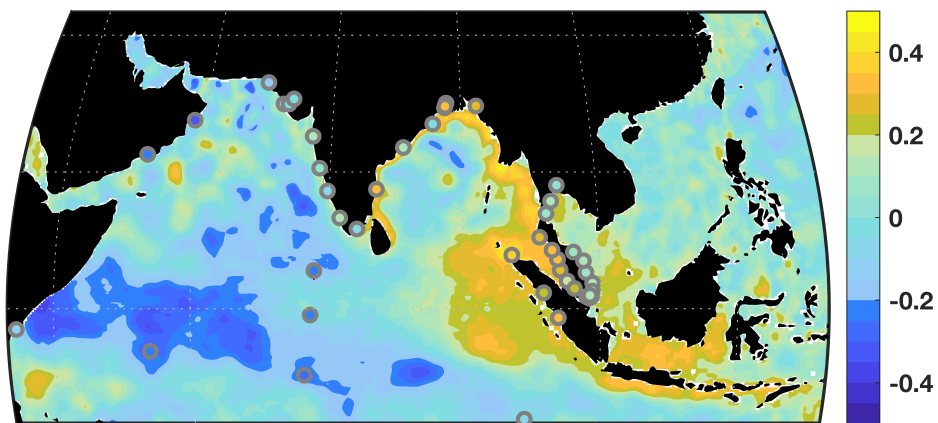
1078 FIG. 8. Shading represents correlation coefficients between Gulf of Oman ζ_0 and ζ from altimetry over the
 1079 Equatorial and North Indian Ocean. Dots are the same, but based on ζ from available tide gauges. Light shading
 1080 indicates values that are not distinguishable from zero at the 95% confidence level (assuming 100 degrees of
 1081 freedom).



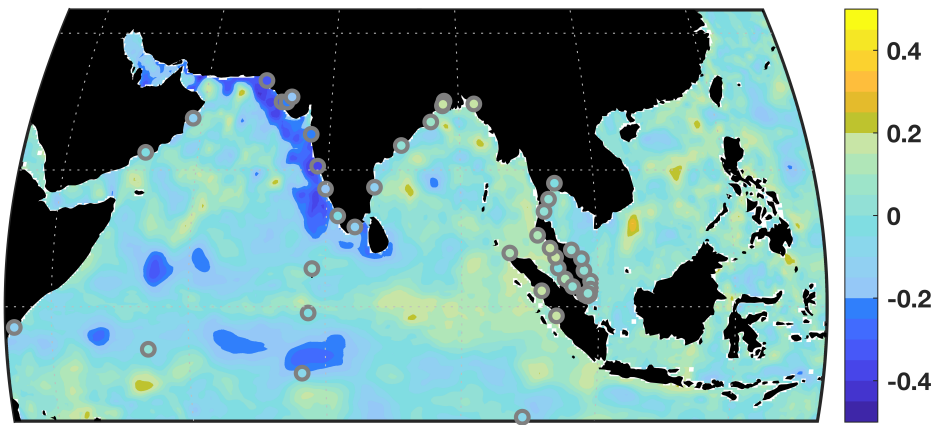
1082 FIG. 9. Shading represents correlation coefficients between Gulf of Oman ζ_0 and $\mathcal{H}(\zeta)$ from altimetry over
1083 the Equatorial and North Indian Ocean. Light shading indicates values that are not distinguishable from zero at
1084 the 95% confidence level (assuming 100 degrees of freedom).



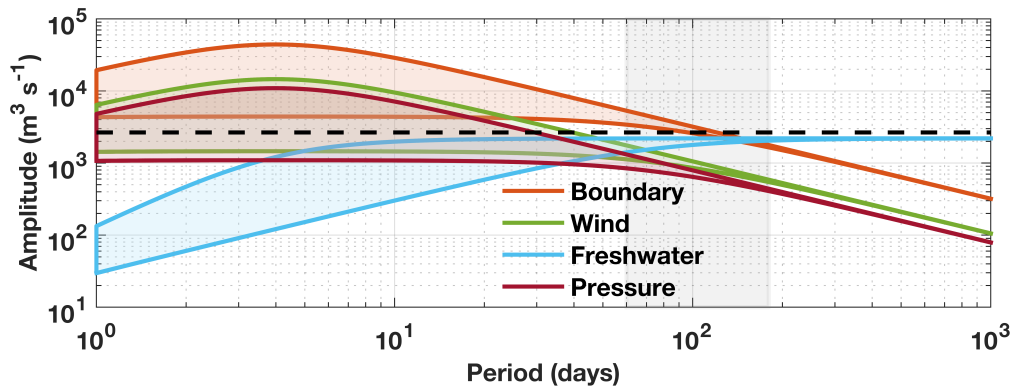
1085 FIG. 10. Correlation coefficient between Gulf of Oman ζ_0 and either (a.) R_m from GRACE or (b.) $\mathcal{H}(R_m)$ over
 1086 the Indian Ocean. Light shading indicates values that are not distinguishable from zero at the 95% confidence
 1087 level (assuming 100 degrees of freedom).



1088 FIG. 11. Shading represents correlation coefficients between Gulf of Oman ζ_0 and altimetric ζ elsewhere over
 1089 the Equatorial and North Indian Ocean 1 month earlier (i.e., ζ_0 is lagging ζ elsewhere). Dots are the same, but
 1090 based on ζ from available tide gauges. Light shading indicates values that are not distinguishable from zero at
 1091 the 95% confidence level (assuming 100 degrees of freedom).



1092 FIG. 12. Shading represents correlation coefficients between Gulf of Oman ζ_0 and altimetric ζ elsewhere over
 1093 the Equatorial and North Indian Ocean 2 months earlier (i.e., ζ_0 is lagging ζ elsewhere). Dots are the same, but
 1094 based on ζ from available tide gauges. Light shading indicates values that are not distinguishable from zero at
 1095 the 95% confidence level (assuming 100 degrees of freedom).



1096 Fig. A1. Amplitude of νWH response to boundary forcing ζ_0 (orange), wind stress τ (green), freshwater
 1097 flux \bar{q} (blue), and barometric pressure \bar{p} (red) as a function of period. Values are based on Eqs. (A4), (A6),
 1098 (A8), (A10) using parameter values from Table 3. Upper and lower lines are bounds determined by the range of
 1099 friction coefficient r . See text for more details. Gray shading indicates intraseasonal periods of primary interest
 1100 here. Dashed black line is the standard deviation of estimated transport described in the Discussion section.